CrossMark

Timing and Spectral Analysis of the Black Hole X-Ray Binary MAXI J1803-298 with Insight-HXMT Data

Ying-Chen Xu[1,2], Jin-Lu Qu[1,2], M. Méndez[3], Rui-Can Ma[1,4], Long Ji[5], Liang Zhang[1], Yue Huang[1] , Qing-Cui Bu[6], and Li-Ming Song[1,2]

[1] Key Laboratory of Particle Astrophysics, Institute of High Energy Physics, Chinese Academy of Sciences, Beijing 100049, China; xuyingchen@ihep.ac.cn, songlm@ihep.ac.cn

[2] University of Chinese Academy of Sciences, Chinese Academy of Sciences, Beijing 100049, China

[3] Kapteyn Astronomical Institute, University of Groningen, P.O. BOX 800, 9700 AV Groningen, The Netherlands

[4] Dongguan Neutron Science Center, Dongguan 523808, China

[5] School of Physics and Astronomy, Sun Yat-Sen University, Zhuhai 519082, China

[6] Institut für Astronomie und Astrophysik, Kepler Center for Astro and Particle Physics, Eberhard Karls Universität, Sand 1, D-72076 Tübingen, Germany

Abstract

We present a comprehensive analysis of the 2021 outburst of MAXI J1803–298 utilizing observations of the Insight-Hard X-ray Modulation Telescope (Insight-HXMT) spanning from the low hard state to the high soft state. Within the Insight-HXMT data set, compared to the previous work, we identify a more prolonged presence of type-C quasi-periodic oscillations (QPOs) with centroid frequencies ranging from ∼0.16 to 6.3 Hz, which present correlations with the hardness ratio and the photon index of the Comptonized component. For QPO frequencies less than ∼2 Hz, the QPO phase lags are hard (photons of 10–19 keV arrive later than those of 1–4 keV), while at higher frequencies, the lags become soft at and above ∼4 Hz. Furthermore, the spectra in all Insight-HXMT observations consist of a multi-color blackbody component and a Comptonized component, as commonly observed in classical black hole X-ray binaries. We analyze state transitions and the evolution of accretion geometry in this work. The fitted inner disk radius increases abnormally during the low hard state, hypothesized to result from the corona condensing onto the inner disk. Additionally, two significant drops in flux are observed during the soft intermediate state, maybe implying changes in the corona/jet and the disk, respectively.

Key words: X-rays: binaries – accretion – accretion disks – stars: black holes

1. Introduction

A black hole X-ray binary (BHXB) normally manifests as an X-ray transient, wherein the majority of its energy is released through accretion onto the central stellar-mass black hole. These systems linger mostly in the quiescent state ($L_X \sim 10^{30}$–10^{33} erg s^{-1}) and show sporadic outbursts with an increase in luminosity of over three orders of magnitude ($L_{X,peak} \sim 10^{36}$–10^{39} erg s^{-1}) (Remillard & McClintock 2006; Tetarenko et al. 2016). A typical BHXB outburst spans dozens of days to several months, during which the source traces a counterclockwise "q" shape in a hardness–intensity diagram (HID) (Fender et al. 2004; McClintock & Remillard 2006; Belloni & Motta 2016). According to its X-ray spectral and timing properties, the entire process can typically be divided into four spectral states. The source transitions from a Comptonized component dominated low-hard state (LHS) to a multi-color blackbody component dominated high-soft state (HSS) via two intermediate states named hard-intermediate state (HIMS) and soft-intermediate state (SIMS) (Remillard & McClintock 2006; Motta et al. 2009; Belloni & Motta 2016). The photon index (Γ) of the Comptonized component varies from ∼1.5 to 1.7 in the LHS, to ∼2.0–2.5 in the HIMS and the SIMS, and up to ∼3 in the HSS (Tetarenko et al. 2016). Meanwhile, a compact, steady jet can be observed in radio in the LHS and the HIMS. This compact jet is replaced by transient relativistic ejections during the transition from the HIMS to the SIMS (Fender et al. 2004).

The shape of the power-density spectrum (PDS) patterns, consisting of quasi-periodic oscillations (QPOs) and noise components, is correlated with the source state (van der Klis 2004; Ingram & Motta 2019). As a BHXB transitions from the hard to the soft state, the noise component changes from a strong flat-topped component to a weaker red noise component (van der Klis 2004). Meanwhile, three classes of low-frequency (LF) QPOs ($\nu_{QPO} \lesssim 30$ Hz), namely type-A, type-B, and type-C, have been identified, primarily classified on the basis of QPO frequency, QPO width, and strength of the noise component (Casella et al. 2005; Motta et al. 2015). Type-C QPOs are the most common ones, usually found in the LHS and the HIMS, characterized by an increasing frequency with the evolution of the source through the outburst, a high QPO fractional root mean square (rms) (up to ∼20%), a narrow

profile ($Q \gtrsim 8$) and a concomitant flat-top noise; type-B QPOs are often present in SIMS, and are characterized by a relatively high QPO rms (up to ~5%) and a narrow profile ($Q \gtrsim 6$), and coupled with a red noise; the weaker (few percent rms) type-A QPOs are generally detected in the soft state, are characterized by a broad profile ($Q \lesssim 3$), appear together with a weak red noise component, and are very uncommon (Ingram & Motta 2019). From the LHS to the HSS, the total rms amplitude decreases from ~30%–40% to ~1% (Belloni & Motta 2016).

Because type-C QPOs are more common and exhibit stronger signals, they are frequently studied. Stiele et al. (2013) showed that the type-C QPO frequency presents a positive correlation with Γ and an anti-correlation with the fraction of up-scattered seed photons into a power law (f_{sc}). Several works have reported that the QPO rms increases with energy, flattening above ~20 keV (Casella et al. 2004; Li et al. 2013; Kong et al. 2020). Motta et al. (2015) suggested that the QPO rms is correlated with the inclination and type-C QPOs are stronger for high-inclination systems. van den Eijnden et al. (2017) found that QPO lags depend on inclination. For QPO frequency $\lesssim 2$ Hz, type-C QPOs present slightly hard lags (high energy photons arrive later than low energy photons), while for higher QPO frequencies, the QPOs present hard and soft lags for low- and high-inclination systems, respectively. Multiple models have been proposed to explain LFQPOs, which fall into two main categories. One category considers the intrinsic variability of the accretion flow, which includes the accretion ejection instability model (Tagger & Pellat 1999), the transition layer model (Titarchuk & Fiorito 2004), the time-dependent Comptonization model (Karpouzas et al. 2020; Bellavita et al. 2022), etc. The other category focuses on Lense–Thirring (LT) precession caused geometric effects, like the inner flow precession model (Ingram et al. 2009) and the small-scale jet precession model (Ma et al. 2021).

MAXI J1803–298 is an X-ray transient source detected by the Gas Slit Camera of the Monitor of All-sky X-ray Image (MAXI/GSC) on 2021 May 1 (Serino et al. 2021). Subsequently, a variety of X-ray telescopes, including the Neil Gehrels Swift Observatory (Swift), the Neutron star Interior Composition Explorer (NICER), the Astronomy Satellite (AstroSat), and the Nuclear Spectroscopic Telescope Array (NuSTAR) initiated follow-up observations of this source. Type-C and type-B QPOs were detected in the PDS of MAXI J1803–298 (Bult et al. 2021; Ubach et al. 2021). Zhu et al. (2023) analyzed both QPO signals using Insight-Hard X-ray Modulation Telescope (Insight-HXMT) and NICER data, respectively. The type-C QPOs they observed are in the LHS, and are detected up to 60 keV, with frequency from ~0.16 to 2.6 Hz. Chand et al. (2022) and Jana et al. (2022) studied the type-C QPOs in the HIMS with AstroSat data. No QPO signals were detected above 30 keV, and the QPO frequency ranges from ~5.3 to 7.6 Hz (Jana et al. 2022).

Coughenour et al. (2023) detected concurrent QPOs of 5.4 ± 0.2 Hz and 9.4 ± 0.3 Hz with NuSTAR data. Additionally, the light curve of this source exhibited pronounced periodic absorption dips (Homan et al. 2021; Xu & Harrison 2021), suggesting that MAXI J1803–298 is a high-inclination system (Frank et al. 1987). Jana et al. (2022) calculated the periodicity of dips to be 7.02 ± 0.18 hr, and estimated the black hole mass to be 3.5–12.5 $M_{\odot}$ through mass function. Meanwhile, spectral analysis, as presented by Chand et al. (2022), suggested a mass of 8.5–16 $M_{\odot}$. Furthermore, using reflection spectroscopy, Feng et al. (2022) and Coughenour et al. (2023) determined an extreme spin value (a high inclination angle) of ~0.991 (~70°) or ~0.988 (~75°) with NuSTAR data of different observations.

Insight-HXMT has observed the complete evolution of MAXI J1803–298 from the LHS to the HSS in its 2021 outburst. We study the timing and spectral properties using the whole Insight-HXMT data to identify the states and the presence of QPO signals (see Zhu et al. 2023). In Section 2, we introduce the data reduction strategy of Insight-HXMT observations and the basic analysis methods. In Section 3, we present our results of timing and spectral analyses. In Sections 4 and 5, we present the discussion and conclusions, respectively.

2. Observations and Data Analysis

2.1. Observations

There are three main scientific payloads on board Insight-HXMT: the Low Energy X-ray Telescope (LE: 1–12 keV—energy coverage, 384 cm^2—effective area, 1 ms—time resolution; Chen et al. 2020; Liao et al. 2020), the Medium Energy X-ray Telescope (ME: 8–35 keV, 952 cm^2, 240 μs; Cao et al. 2020; Guo et al. 2020), and the High Energy X-ray Telescope (HE: 20–350 keV, ~5100 cm^2, 4 μs; Liu et al. 2020). The small fields of view (FoVs) are $1°.6 \times 6°$, $1° \times 4°$ and $1°.1 \times 5°.7$ for the LE, ME and HE, respectively. Following the discovery of MAXI J1803–298 with MAXI/GSC, Insight-HXMT observations were carried out from MJD 58337 to MJD 59423. More information on the observation times is given in Table 1.

2.2. Data Reduction

We processed the primary data using the HPIPELINE task from the Insight-HXMT Data Analysis Software package (HXMTDAS) v2.05,[7] which integrates all modules of the HXMTDAS for LE, ME, and HE. This task first produces screened event FITS files (screened files) through calibration and screening and then extracts high-level scientific products, i.e., light curves, spectra, response files and background files of light curves and spectra. The parameters of this task are

---

7 http://hxmtweb.ihep.ac.cn/software.jhtml

Table 1
Insight-HXMT Observations of MAXI J1803–298

expID	MJD-OBS	Exposure (ks)			LE Box	expID	MJD-OBS	Exposure (ks)			LE Box	expID	MJD-OBS	Exposure (ks)			LE Box
		LE	ME	HE				LE	ME	HE				LE	ME	HE	
0101	59337.7	1.5	3.3	2.3	02	1007	59348.1	···	0.9	0.4	02	1802	59359.0	0.7	1.8	2.4	0
0201	59338.5	2.2	3.5	3.7	02	1008	59348.2	···	1.7	1.8	02	1901	59359.8	1.3	2.7	2.6	0
0301	59339.7	3.0	3.3	3.1	02	1009	59348.3	···	1.7	2.5	02	2001	59360.8	1.6	2.8	2.7	0
0302	59339.9	1.3	0.9	1.5	02	1010	59348.5	···	1.4	0.3	02	2101	59361.9	1.6	1.9	0.0	0
0401	59340.6	2.7	3.3	1.7	02	1011	59348.6	···	2.1	3.4	02	2102	59362.0	1.1	1.8	2.7	0
0402	59340.8	1.3	1.0	1.6	02	1012	59348.7	0.1	2.1	3.1	02	2103	59362.2	0.6	1.2	0.2	0
0701	59341.5	1.7	3.2	3.1	02	1013	59348.9	···	1.5	2.4	02	2201	59363.0	1.1	1.9	1.8	0
0702	59341.7	1.1	2.1	1.8	02	1014	59349.0	···	0.4	0.6	02	2202	59363.1	1.0	1.5	1.3	0
0703	59341.8	2.3	2.2	3.2	02	1101	59349.3	···	2.3	3.4	02	2203	59363.2	0.5	0.8	0.0	0
0704	59341.9	1.6	1.9	2.7	02	1102	59349.5	···	1.3	0.7	02	2301	59363.9	1.3	2.0	2.2	0
0705	59342.1	0.6	0.5	0.9	02	1103	59349.6	0.2	2.2	3.3	02	2302	59364.1	1.1	1.4	1.2	0
0706	59342.2	···	0.4	0.3	02	1104	59349.7	0.1	1.9	3.1	02	2303	59364.2	0.6	0.8	0.2	0
0707	59342.3	1.3	1.9	2.2	02	1105	59349.9	···	1.3	1.9	02	2501	59364.9	1.1	2.0	0.9	0
0708	59342.5	0.6	2.2	3.3	02	1106	59350.0	0.1	0.9	0.7	02	2502	59365.0	1.3	1.6	2.5	0
0709	59342.6	0.9	1.9	0.4	02	1107	59350.1	···	1.4	1.2	02	2503	59365.1	0.9	0.9	···	0
0710	59342.7	0.9	2.3	3.3	02	1108	59350.3	···	1.8	2.7	02	2601	59365.9	1.5	2.1	1.1	0
0711	59342.8	0.6	2.1	3.1	02	1109	59350.4	···	1.2	0.7	02	2602	59366.0	1.4	1.6	2.1	0
0712	59343.0	1.2	1.3	2.0	02	1110	59350.5	0.1	1.5	2.5	02	2603	59366.1	1.0	0.9	···	0
0713	59343.1	···	0.3	0.3	02	1111	59350.7	0.4	2.2	3.2	02	2701	59366.8	1.8	2.1	···	0
0801	59343.5	0.6	2.8	1.3	02	1112	59350.8	0.1	1.8	2.6	02	2702	59366.9	1.6	1.8	2.5	0
0802	59343.6	0.4	2.1	1.7	02	1113	59350.9	0.1	0.9	1.1	02	2703	59367.1	1.3	1.1	0.4	0
0803	59343.8	0.9	2.2	2.7	02	1114	59351.1	···	1.1	0.1	02	2801	59367.8	1.6	2.1	···	0
0804	59343.9	0.2	1.7	2.6	02	1115	59351.2	···	2.0	2.9	02	2802	59367.9	1.1	1.7	2.4	0
0805	59344.0	···	0.5	0.5	02	1116	59351.3	···	1.3	1.1	02	2803	59368.1	0.8	1.0	0.1	0
0806	59344.2	0.2	0.6	0.2	02	1201	59351.7	0.2	2.8	4.1	02	2901	59369.0	1.3	1.5	0.9	0
0807	59344.3	0.3	2.0	2.8	02	1202	59351.9	···	0.7	1.1	02	3001	59369.8	1.6	2.5	2.1	0
0808	59344.4	0.1	2.0	2.2	02	1301	59352.0	0.5	1.0	0.9	02	3101	59370.9	1.6	1.8	1.8	0
0809	59344.6	···	1.8	1.2	02	1302	59352.1	···	1.7	1.1	02	3201	59371.9	1.7	2.0	1.8	0
0810	59344.7	0.3	2.3	3.3	02	1303	59352.2	···	1.9	2.8	02	3301	59373.4	2.2	2.7	4.0	0
0811	59344.8	···	2.1	3.0	02	1304	59352.4	···	1.1	0.0	02	3401	59374.9	1.8	1.4	1.1	01
0812	59345.0	···	0.7	1.1	02	1305	59352.5	0.4	2.0	3.4	02	3402	59375.0	0.9	0.8	···	01
0901	59345.3	0.2	2.8	4.1	02	1401	59352.7	0.5	2.8	4.3	02	3601	59378.1	1.1	2.3	3.4	01
0902	59345.5	···	1.7	···	02	1402	59352.9	0.3	1.3	1.9	02	3701	59379.5	3.2	2.8	0.8	0
0903	59345.6	···	2.2	3.4	02	1403	59353.0	0.4	1.1	0.0	02	3801	59387.5	3.8	4.8	4.5	2
0904	59345.8	0.2	2.2	3.1	02	1404	59353.1	0.1	1.5	1.8	02	4001	59391.1	1.6	1.6	2.6	01
0905	59345.9	···	1.8	2.6	02	1405	59353.2	···	1.6	2.1	02	4101	59393.7	3.0	2.4	2.0	1
0906	59346.0	···	0.6	0.6	02	1406	59353.4	···	0.9	0.2	02	4201	59396.7	2.8	2.3	3.9	1
0907	59346.2	···	0.8	0.3	02	1407	59353.5	0.5	2.2	3.2	02	4301	59397.7	2.9	2.7	3.9	1
0908	59346.3	···	2.0	2.9	02	1408	59353.6	0.5	1.9	2.7	02	4401	59399.7	1.2	1.7	3.5	1
0909	59346.4	···	1.7	1.3	02	1409	59353.8	0.5	1.6	2.4	02	4501	59401.7	0.6	2.1	3.9	1
0910	59346.6	···	1.8	1.8	02	1410	59353.9	0.6	1.2	0.9	02	4601	59406.4	···	3.1	2.1	1
0911	59346.7	···	2.2	3.2	02	1411	59354.0	0.3	1.3	0.7	02	4701	59407.5	0.1	2.7	3.7	1
0912	59346.8	···	2.0	3.0	02	1412	59354.2	···	1.8	2.5	02	4801	59409.7	0.2	1.8	2.7	1
0913	59347.0	···	0.7	1.1	02	1413	59354.3	···	1.1	0.7	02	4901	59411.7	0.5	2.0	2.8	01
1001	59347.2	···	2.3	3.0	02	1501	59355.3	···	1.7	1.0	02	5001	59413.8	0.6	1.6	0.9	01
1002	59347.4	···	1.6	1.2	02	1601	59356.5	0.8	2.8	3.8	0	5101	59415.8	1.1	1.9	0.9	01
1003	59347.5	···	1.8	1.9	02	1701	59357.7	0.7	1.8	2.7	0	5201	59418.7	1.5	1.7	2.4	01
1004	59347.7	···	2.0	3.2	02	1702	59357.8	0.5	1.6	2.3	0	5301	59419.9	1.7	2.7	2.6	01
1005	59347.8	···	1.9	2.9	02	1703	59357.9	1.7	2.5	1.4	0	5501	59423.3	1.4	2.8	4.2	01
1006	59348.0	···	1.1	1.6	02	1801	59358.9	0.8	1.7	0.3	0						

Note. (1) An expID P03040140**** is abbreviated as ****. (2) An exposure time with "···" represents an empty GTI. (3) Box 0, 01, 02 mean that we only used the data of box-0, box-0 and box-1, box-0 and box-2, respectively.

explained in the *HXMT Data Reduction Guide*[8] *for hxmtsoftv2.05*. We employed default parameters in our data reduction process and only applied small FoVs to minimize potential contamination from the bright Earth and nearby sources of the MAXI J1803–298.

During the observations of MAXI J1803–298, there were four persistent sources (GX 5–1, NGC 6624, GX 3+1, and 1A 1742–294) and one source (GRS 1739–278) with weak bursts in the small FoVs of Insight-HXMT (see Figure 1). The maximum flux values for these sources are provided in Table 2. In the case of the small FoVs of LE, we computed the light curves for each Detector Box (DetBox) and found that contaminating sources contributed to more than 3% of the total flux for all Exposure IDs (expIDs).[9] Consequently, we excluded data from the significantly contaminated DetBox. For ME, which has smaller FoVs, 1A 1742–294 was the strongest contaminating source, contributing to less than ∼1% of the total flux. In the case of HE, the flux contribution of GX 5–1 was negligibly small, at less than 1%, and NGC 6624 was outside the FoV for the expIDs we used. Therefore, we opted to dismiss potential contamination effects for both ME and HE. Details about the specific DetBoxes used for each observation in the LE data can be found in Table 1.

To minimize the impact of periodic dips every ∼7 hr on data, we first identified dip periods via lower count rates (2–10 keV) and higher hardness ratio ((4–10 keV)/(2–4 keV)) of LE and checked the periodicity of dips; we then filtered out the dip periods in the GTI files and regenerated screened files and high-level scientific products.

2.3. Timing and Spectral Analysis

We derived a PDS for each expID through screened files using the task POWSPEC within FTOOLS. Following the initial determination, the PDSs were calculated in two distinct time segments based on the approximate QPO frequencies and were converted to fractional rms normalization (Belloni & Hasinger 1990). To study the QPO at frequencies <1 Hz, we computed PDSs in the 1/128–32 Hz range. For the QPO frequencies >1 Hz, considering shorter exposure times of LE, we computed PDS in the 1/32–32 Hz range. The PDSs were then fitted using XSPEC v12.11.1 with a sum of Lorentzian functions. Due to the continuous presence of QPO signals, we moderately relaxed the confidence level. We define a QPO signal only if its Q factor ($Q = \nu/\mathrm{FWHM}$) > 2 and its significance[10] >2.58σ. We determined the rms over the 1/32–32 Hz frequency range, accounting for the background

---

[8] http://hxmtweb.ihep.ac.cn/SoftDoc.jhtml

[9] ExpID is used to name the directory of exposure data, we used a short format of it. For example, P030401400101 indicates it is the 1st exposure of the observation P0304014001.

[10] The significance of QPOs is given as the ratio of the norm of the Lorentzian used to fit the QPO divided by its 1σ error.

influence as detailed in Belloni & Hasinger (1990). We calculated the QPO phase lags using the method of Vaughan & Nowak (1997) and Yang et al. (2022). Essential information about QPOs can be found in Table 3, with all reported errors provided at the 1σ level.

In terms of the spectral analysis, we rebinned the spectra to a minimum of 50 counts per bin with the task GRPPHA in FTOOLS. We adopted the energy bands of 2.0–10.0 keV, 10.0–28.0 keV, and 28.0–100.0 keV for LE, ME, and HE, respectively. However, due to the diminishing fluxes in ME and HE, we reselected the energy bands of 10.0–20.0 keV for ME and did not use HE data after MJD 59361, and only used LE data after MJD 59370. After MJD 59380, likely due to the reduced count rate, the spectral parameters cannot be constrained well. As such, observations after this date are excluded in our analysis. We used the χ^2 statistics and incorporated a systematic uncertainty of 1% in the model in XSPEC. To account for the calibration differences among the three instruments, we introduced a multiplicative factor to the model. We kept this factor fixed at 1 for LE and let it be free for ME and HE. In modeling Galactic absorption, we chose the component TBabs with abundances as in Wilms et al. (2000) and cross-section as in Verner et al. (1996). The absorption column density cannot be adequately constrained by the Insight-HXMT data because the LE energy band starts at 2 keV. We therefore fixed the parameter N_{H} at 0.32×10^{22} cm^{-2} as reported with NICER data (Bult et al. 2021) in the following analysis.

3. Results

3.1. Timing Evolution

Figure 2 presents the HID using MAXI/GSC data from MJD 59335 to MJD 59570 and all Insight-HXMT data from MJD 59337 to MJD 59424 in the top panel. The vertical axis is the count rate in the 2–10 keV band, and the horizontal axis is the hardness ratio defined as the ratio of the 4–10 keV to the 2–4 keV count rates. The relatively complete HID using the MAXI/GSC data (gray points) exhibits a pattern similar to that of the BHXBs, following a counterclockwise q-shape. The Insight-HXMT data, depicted in blue, black, green, and red corresponding, respectively, to the LHS, HIMS, SIMS and HSS, as later, parallel the trend in the MAXI/GSC data. However, in this case, Insight-HXMT did not capture the transition of the source back to the LHS. In the bottom panel of Figure 2, we show the hardness–rms diagram (HRD). The vertical axis is the total fractional rms in the 2–10 keV band calculated in the 1/32–32 Hz range. The rms amplitude first decreases with decreasing hardness ratio from ∼30% to ∼10%, and then remains at a low level. From both panels, it is apparent that the blue points exhibit rapid variations of count rate and total fractional rms with a subtle hardness ratio change.

Figure 3 presents the light curves, hardness ratio and total fractional rms amplitude with the Insight-HXMT data. In the initial 7 days, the LE count rate increases whereas the ME, HE,
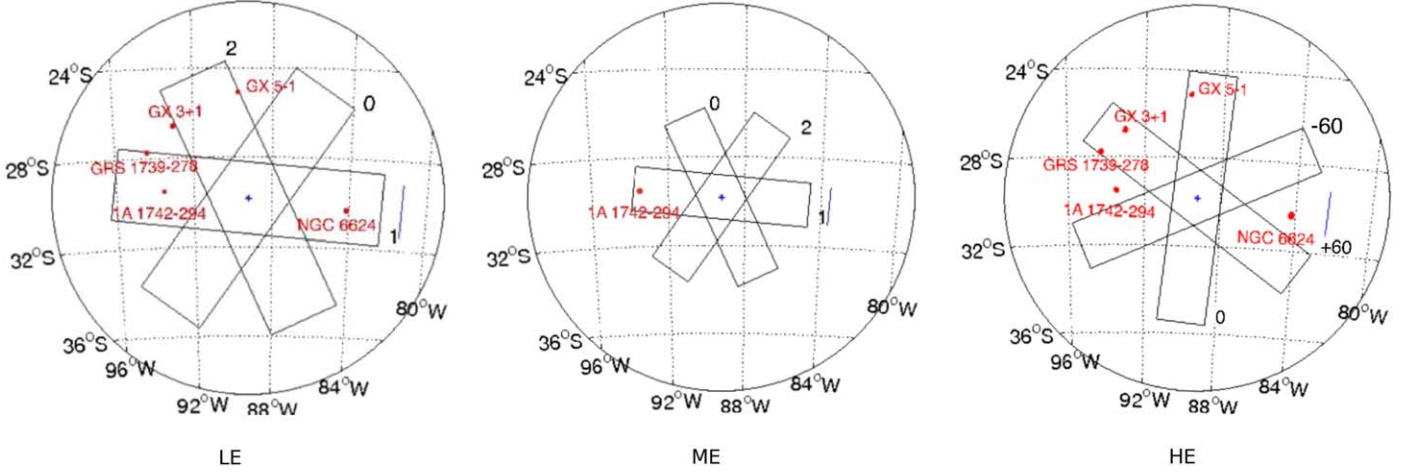
Figure 1. The small FoVs of Insight-HXMT and the location of five contaminating sources on MJD 59337. MAXI J1803–298 is the blue cross at the center of the images.

and the hardness ratio decrease with time. In all cases there is a break in the slope of these relations: the increasing/decreasing trends are slower in the first 3 days than in the following 4 days. After 7 days, all the light curves and hardness ratio values show a similar evolutionary trend. The count rate of LE reaches a peak of 2.0 cts s^{-1} cm^{-2} in 12 days and then shows large-scale fluctuating behavior twice before decreasing in 10 days. The total fractional rms presents a decreasing trend at first, with a smaller slope declining from $\sim$30% to 20%, then dropping to under 10% in 7 days. After this time, the total fractional rms remains at a low level, below 10%, albeit with larger errors, except during the second flux drop.

3.2. QPO Properties

QPOs are detected in the initial 9 days of the Insight-HXMT data. In Figure 4, we present the centroid frequency of the QPOs as a function of time. The black and gray points represent Insight-HXMT data in the 10–28 keV and AstroSat data in the 3–6 keV band (Jana et al. 2022), respectively. There are slight differences between the QPO frequencies detected in the Insight-HXMT and AstroSat data due to the incomplete consistency of the observing times. Referring to Figure 3 in Chand et al. (2022), the frequency presents slight fluctuations. This figure shows that the QPO frequency increases with time from $\sim$0.16 to 6.3 Hz in the first 8 days, then decreases to $\sim$5.3 Hz in 1 day, and finally increases again up to $\sim$7.5 Hz. Referring to Figure 3, the QPO frequency increases accompanied by a softening of the spectrum. Before MJD 59344, the QPO signal is more significant, and we detect a QPO signal up to 60 keV for a few expIDs. From MJD 59344 to MJD 59346, the QPO is observed for most expIDs in the ME (10–28 keV). However, the QPO is only detected in a few HE (28–100 keV)

Table 2
The Maximum Flux Density of the Five Contaminating Sources During the Outburst of MAXI J1803–298

	Flux Density (mCrab)		
	2–10 keV (MAXI/GSC)	10–20 keV (MAXI/GSC)	15–50 keV (Swift/BAT)
GX 5–1	2661	1055	151
NGC 664	937	519	104
GX 3+1	366	211	41
1A 1742–294	225	252	52
GRS 1739–278	140	76	19

expIDs. As for LE (1–10 keV), the QPO is rarely observed, presumably because of the short exposure time. In Table 3, we present the centroid frequency, FWHM, and fractional rms of the QPO for each expID. Figure 5 shows examples of fitted PDS in three detectors for expID P030401400101 and P030401400712.

In Figure 6, we present the QPO rms as a function of QPO frequency in three energy bands: LE (1–10 keV), ME (10–28 keV) and HE (28–100 keV). The rms of the QPO in the LE band decreases, whereas that in ME and HE increases with QPO frequency for QPO frequency $\lesssim$1 Hz. Above this QPO frequency, they all remain more or less constant. We fitted them with a function:

$$
\begin{aligned}
\text{rms}_{\text{QPO}} &= a \cdot f_{\text{QPO}} + b \quad f_{\text{QPO}} < f_0 \\
\text{rms}_{\text{QPO}} &= a \cdot f_0 + b \qquad f_{\text{QPO}} \geqslant f_0
\end{aligned}
, \qquad (1)
$$

where rms_{QPO} and f_{QPO} represent QPO rms and QPO frequency, respectively. For the LE data we get $a = -7 \pm 3\%$/Hz, $b = 14\% \pm 1\%$, $f_0 = 1.0 \pm 0.2$ Hz and χ^2/dof =

Table 3
The Fitted Parameters of Type-C QPOs for Three Detectors

ExpID	QPO Frequency (Hz)			FWHM (Hz)			QPO rms (%)		
	LE	ME	HE	LE	ME	HE	LE	ME	HE
0101	0.161 ± 0.005	0.160 ± 0.002	0.162 ± 0.002	0.04 ± 0.01	0.026 ± 0.008	0.022 ± 0.004	12 ± 1	11.1 ± 0.8	11.9 ± 0.9
0201	0.223 ± 0.006	0.224 ± 0.005	0.222 ± 0.003	0.08 ± 0.02	0.07 ± 0.02	0.029 ± 0.005	12 ± 1	12 ± 2	12.8 ± 0.8
0301	0.38 ± 0.01	0.380 ± 0.005	0.378 ± 0.003	0.18 ± 0.06	0.07 ± 0.02	0.064 ± 0.009	12 ± 2	11.6 ± 0.9	14.6 ± 0.6
0302	0.394 ± 0.009	0.410 ± 0.007	0.39 ± 0.01	0.09 ± 0.03	0.08 ± 0.02	0.07 ± 0.03	11 ± 1	14 ± 1	14 ± 1
0401	0.59 ± 0.01	0.606 ± 0.007	0.635 ± 0.005	0.18 ± 0.04	0.08 ± 0.02	0.07 ± 0.01	10.6 ± 0.9	12.4 ± 0.8	14.6 ± 0.9
0402	0.71 ± 0.02	0.67 ± 0.02	0.678 ± 0.006	0.11 ± 0.06	0.07 ± 0.04	0.09 ± 0.02	8 ± 1	12 ± 2	17 ± 1
0701	1.48 ± 0.01	1.43 ± 0.02	1.47 ± 0.01	0.07 ± 0.04	0.31 ± 0.05	0.17 ± 0.03	7 ± 1	20 ± 1	20 ± 1
0702	1.53 ± 0.03	1.55 ± 0.02	1.63 ± 0.01	0.2 ± 0.1	0.29 ± 0.06	0.23 ± 0.04	7 ± 1	18 ± 1	22 ± 1
0703	1.72 ± 0.02	1.77 ± 0.02	1.74 ± 0.01	0.26 ± 0.05	0.33 ± 0.09	0.29 ± 0.04	8.8 ± 0.6	17.8 ± 1.4	20.9 ± 0.8
0704	1.89 ± 0.01	1.94 ± 0.02	1.91 ± 0.01	0.10 ± 0.05	0.25 ± 0.05	0.25 ± 0.04	6.1 ± 0.6	18 ± 1	20.4 ± 0.9
0705	*	*	*	*	*	*	*	*	*
0706	⋯	2.00 ± 0.06	2.03 ± 0.05	⋯	0.5 ± 0.4	0.2 ± 0.1	⋯	22 ± 3	14 ± 3
0707	2.05 ± 0.04	2.07 ± 0.02	2.04 ± 0.02	0.3 ± 0.1	0.33 ± 0.07	0.28 ± 0.08	7.5 ± 0.9	20 ± 1	20 ± 2
0708	*	2.15 ± 0.02	2.17 ± 0.02	*	0.19 ± 0.05	0.26 ± 0.05	*	15 ± 1	20 ± 1
0709	2.20 ± 0.05	2.19 ± 0.04	*	0.2 ± 0.1	0.5 ± 0.2	*	7 ± 1	21 ± 2	*
0710	2.6 ± 0.1	2.58 ± 0.04	2.55 ± 0.02	0.6 ± 0.3	0.6 ± 0.2	0.33 ± 0.06	8 ± 2	20 ± 1	20 ± 1
0711	2.87 ± 0.09	2.78 ± 0.04	2.78 ± 0.03	0.5 ± 0.2	0.4 ± 0.1	0.32 ± 0.09	8.7 ± 0.9	19 ± 2	18 ± 2
0712	2.97 ± 0.07	2.89 ± 0.08	2.98 ± 0.08	0.6 ± 0.9	0.4 ± 0.3	0.7 ± 0.3	6 ± 2	19 ± 3	25 ± 3
0713	⋯	*	*	⋯	*	*	⋯	*	*
0801	*	3.13 ± 0.05	*	*	0.6 ± 0.2	*	*	20 ± 2	*
0802	3.6 ± 0.1	3.53 ± 0.04	3.43 ± 0.03	0.6 ± 0.2	0.7 ± 0.2	0.3 ± 0.1	7 ± 1	22 ± 2	16 ± 2
0803	3.67 ± 0.07	3.65 ± 0.05	3.59 ± 0.06	0.3 ± 0.1	0.6 ± 0.2	0.6 ± 0.2	5.9 ± 0.7	22 ± 2	24 ± 3
0804	*	3.70 ± 0.03	3.65 ± 0.06	*	0.30 ± 0.06	0.7 ± 0.2	*	18 ± 1	19 ± 2
0805	⋯	*	*	⋯	*	*	⋯	*	*
0806	*	3.7 ± 0.1	*	*	0.2 ± 0.1	*	*	15 ± 3	*
0807	*	4.39 ± 0.08	4.3 ± 0.1	*	0.9 ± 0.2	0.8 ± 0.6	*	23 ± 2	17 ± 5
0808	*	5.1 ± 0.2	*	*	0.9 ± 0.5	*	*	21 ± 3	*
0809	⋯	4.9 ± 0.2	*	⋯	1.4 ± 0.5	*	⋯	23 ± 2	*
0810	*	5.42 ± 0.07	5.8 ± 0.2	*	0.7 ± 0.2	1.1 ± 0.5	*	20 ± 2	19 ± 3
0811	⋯	*	6.1 ± 0.1	⋯	*	0.7 ± 0.3	⋯	*	19 ± 3
0812	⋯	5.64 ± 0.06	*	⋯	0.4 ± 0.2	*	⋯	19 ± 2	*
0901	*	6.1 ± 0.1	*	*	1.0 ± 0.4	*	*	18 ± 2	*
0902	⋯	6.16 ± 0.06	⋯	⋯	0.3 ± 0.2	⋯	⋯	14 ± 2	⋯
0903	⋯	6.33 ± 0.07	*	⋯	0.6 ± 0.2	*	⋯	18 ± 2	*
0904	*	5.83 ± 0.08	*	*	0.7 ± 0.3	*	*	16 ± 2	*
0905	⋯	5.9 ± 0.1	*	⋯	0.9 ± 0.3	*	⋯	19 ± 2	*
0906	⋯	*	*	⋯	*	*	⋯	*	*
0907	⋯	*	*	⋯	*	*	⋯	*	*
0908	⋯	5.24 ± 0.06	5.1 ± 0.1	⋯	0.6 ± 0.3	0.8 ± 0.3	⋯	18 ± 2	19 ± 3
0909	⋯	5.1 ± 0.2	*	⋯	1.6 ± 0.5	*	⋯	25 ± 2	*

Note. The LE, ME and HE represent the 1–10 keV (LE), 10–28 keV (ME), and 28–100 keV (HE) energy bands of Insight-HXMT respectively. QPO information with "⋯" represents empty GTI, while that with "*" means that no QPO with significance greater than 99.0% is detected.

21.3/14. For ME and HE data, we get $a = 6 \pm 1\%/$Hz, $b = 11\% \pm 1\%$, $f_0 = 1.4 \pm 0.2$ Hz and $\chi^2/$dof = 97.9/54. The fitting results are displayed in Figure 6. In Figure 7, we present the QPO phase lags for the energy band 10–19 keV (ME) with respect to the 1–4 keV energy band (LE). Black and red points represent QPO lags calculated from the Insight-HXMT data and the result reported by Chand et al. (2022), respectively. To better reveal the evolutionary trend, we rebinned the results of Insight-HXMT marked as blue points. The QPO lags first increase and then decrease with frequency, with ∼1 Hz as the turning point. The figure shows relatively strong hard QPO lags when QPO frequency ≲2 Hz, approaching zero lags beyond this frequency. Combined with the result of soft QPO lags reported by Chand et al. (2022), the Insight-HXMT data are consistent with soft QPO lags when the QPO frequency is above ∼4 Hz.
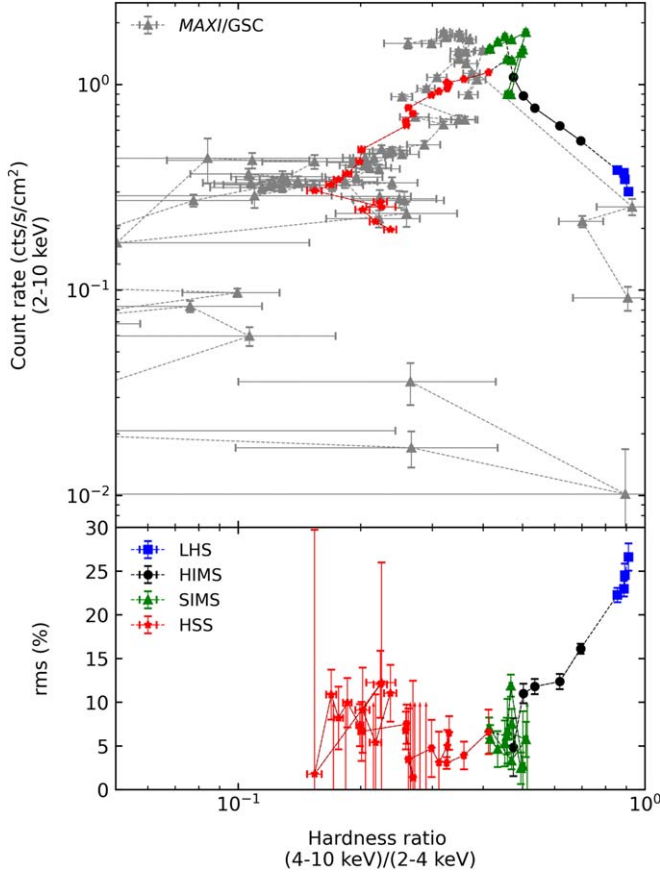
Figure 2. Top panel: HID of MAXI J1803–298 using MAXI/GSC data from MJD 59335 to MJD 59570 (gray) and all Insight-HXMT data. The horizontal axis is the hardness ratio of the 4–10 keV to 2–4 keV count rate, while the vertical axis is the count rate of 2–10 keV. Bottom panel: HRD of MAXI J1803–298 using all Insight-HXMT data. The vertical axis is the total fractional rms calculated in the 1/32–32 Hz range. In both panels, blue, black, green, and red points correspond to Insight-HXMT data when the source is in the LHS, HIMS, SIMS, and HSS states, respectively.

3.3. Energy Spectra

To compare with the results of Jana et al. (2022), we fitted the corresponding energy spectra with a similar model, constant $*$ TBabs $*$ (diskbb+nthcomp) (model 1). In this model, we linked the seed photon temperature of the nthcomp model to the temperature at the inner disk radius (T_{in}) of the diskbb model. However, the inner disk radius, r_{in}, is not constrained well during the LHS and HIMS, and we finally refitted with the model constant $*$ TBabs $*$ (simplcutx $*$ diskbb) (model 2). In this model, we chose the scattering kernel which is shaped by an exponential cutoff. We also tried to change the scattering kernel of model 2 based upon nthcomp and got similar results with model 1. In Figure 8, we present examples of the fits with the two models for four states. A weak iron line component left in the residuals of the spectral data can be seen

in the bottom panel of each subplot. We use the task SIMFTEST in XSPEC to test its significance with 10,000 simulations and get a significance of less than 3σ. Therefore, the iron line component was not taken into account in our fitting.

We present the evolution of the best-fitting parameters in Table 4 and Figure 9. In Figure 9, red and blue dots symbolize the results with model 1 and model 2, respectively, while the gray dots show the results from Jana et al. (2022). For model 2, assuming a distance to the source $d = 8$ kpc and an inclination angle $i = 70°$, r_{in} increases with time in the initial 4 days from 45 ± 6 km to 115 ± 10 km, and then decreases to a relatively low value of 42.4 ± 0.4 km after 5 days. However, there is a subtle uptrend of r_{in} following a minor fluctuation corresponding to the second significant drop in the light curve on MJD 59357. Showing an opposite evolutionary trend with respect to r_{in}, T_{in} decreases from $\sim$0.5 to 0.4 keV on MJD 59341 and then increases up to $\sim$1 keV on MJD 59348. The power-law photon index, Γ, initially increases over time, starting at $\sim$1.3 and reaching $\sim$2.4 in 9 days. It then remains relatively stable between $\sim$2.0 and 2.6 between MJD 59348 and MJD 59368 before increasing to $\sim$5. The exponential cutoff energy (E_{cut}) fluctuates between $\sim$40 keV and 80 keV, but after 4 days it exhibits a clear increase despite relatively large errors. We fixed E_{cut} at 500 keV after the initial 9 days. The scattering factor of the diskbb component (f_{sc}) initially shows an opposite trend to r_{in}, being $\sim$0.4 in the first 9 days. However, corresponding to the first significant drop in the light curve, f_{sc} presents a significant drop with a valley value of $\sim$0.2. After 25 days from the first observation, f_{sc} decreases to a low level of $\sim$0.1. The proportion of the diskbb component flux (f_{dbb}) demonstrates an increasing trend for the first 9 days, from a low level of $\sim$0.12, then displays a strong trend opposite to that of f_{sc}, reaching up to $\sim$0.85. The unabsorbed bolometric flux in the 1–100 keV follows a similar pattern to the light curve of LE, peaking at $\sim 2.2 \times 10^{-8}$ erg cm^{-2} s^{-1}.

4. Discussion

In this paper, we investigate the timing and spectral properties of MAXI J1803–298 during the 2021 outburst using Insight-HXMT observations. Based on the HID pattern, the detected QPO frequencies and spectral components, MAXI J1803–298 aligns with the characteristics of a BHXB.

4.1. Type-C QPOs

Insight-HXMT observed an evolving type-C QPO signal with frequencies ranging from $\sim$0.16 to 6.3 Hz. No QPO signal is detected after MJD 59346, possibly due to a decrease in the QPO rms. There are two turning points of QPO frequency in Figure 4 between MJD 59345 and MJD 59347. Works by Chand et al. (2022) and Jana et al. (2022) have indicated a relationship between QPO frequency and count rate (hardness ratio). Meanwhile, similar turning points in parameters T_{in}, r_{in}, Γ and f_{sc} are observed compared to QPO
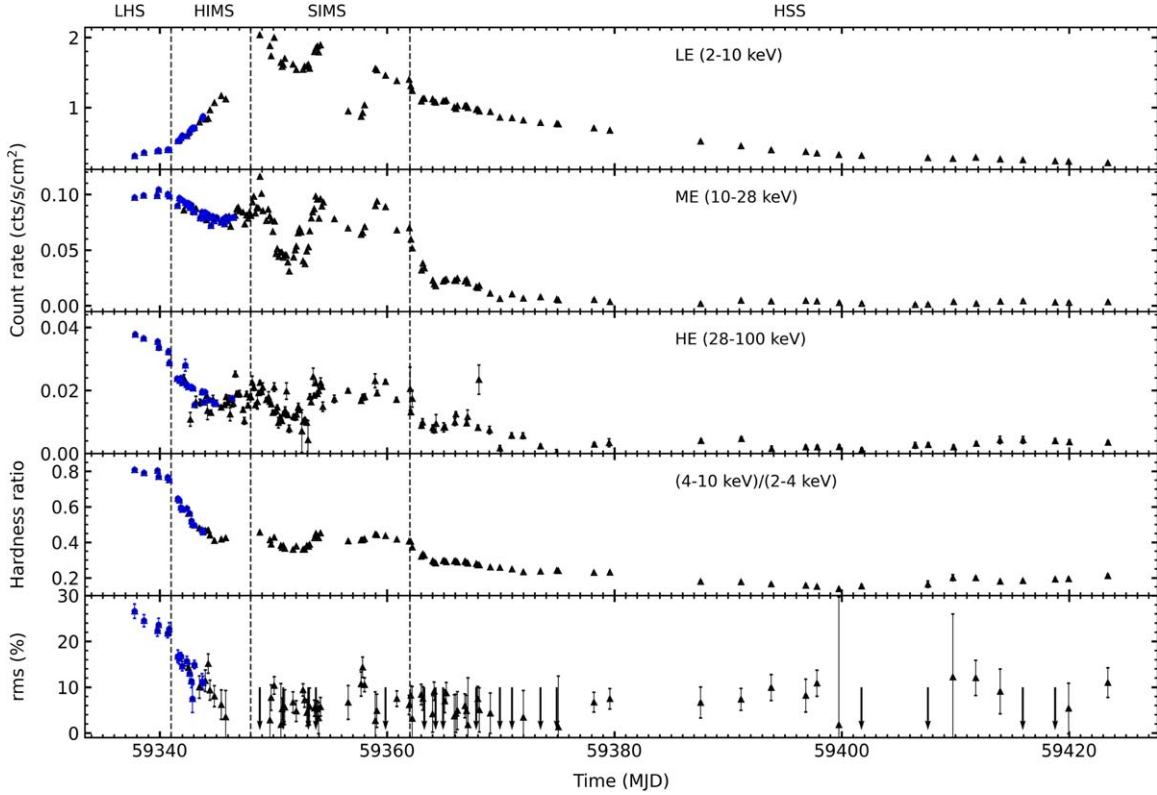
Figure 3. Light curves, hardness ratio, and total fractional rms evolution for MAXI J1803–298 using Insight-HXMT data before MJD 59423. Top three panels: net light curves for LE (1–10 keV), ME (10–28 keV), and HE (28–100 keV), from top to bottom respectively. Fourth panel: the evolution of the hardness ratio for LE (4–10 keV over 2–4 keV count rates). Bottom panel: total fractional rms calculated in the 1/32–32 Hz range. The blue dots represent the intervals in which the type-C QPOs are detected. The vertical lines signify the moment of the state transitions.
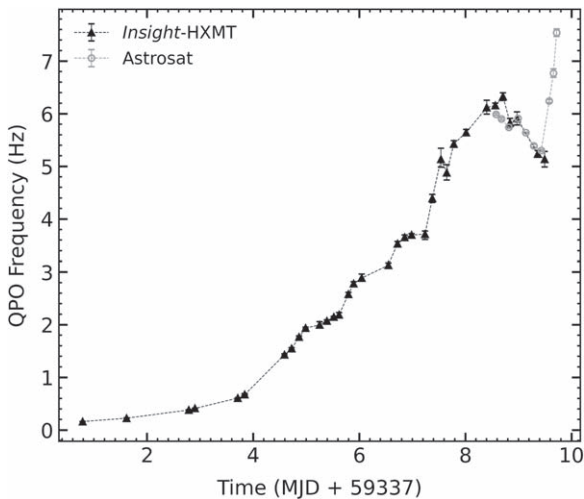

Figure 4. QPO frequency as a function of the time for MAXI J1803–298. The black symbols represent an expID of ME (10–28 keV). The QPO frequency (6–12 keV) from Jana et al. (2022) is also shown as gray points.

frequency, as reported by Jana et al. (2022). In Figure 10, we present a relation between the hardness ratio and Γ as functions of QPO frequency, showing monotonically decreasing and increasing relationships, respectively. Casella et al. (2005) suggested that the three types of LFQPOs in BHXBs correspond to the three branch oscillations in high-luminosity neutron star systems (Hasinger & van der Klis 1989), in which type-C QPOs correspond to the horizontal branch oscillations. Based on the concomitant flat-top noise, the intensity-dependent QPO frequency, and the anti-correlation between QPO frequency and total rms, it is possible that the QPO of black hole and neutron systems are generated by similar physical mechanisms.

The inner flow precession model, based on the truncated disk model (Esin et al. 1997; Done et al. 2007), proposes that type-C QPOs originate from the LT precession of the entire inner flow, an outcome of the misalignment of the spin axis with that of the black hole (Ingram et al. 2009). In this model, the QPO frequency is related to the size of the corona. During the rising
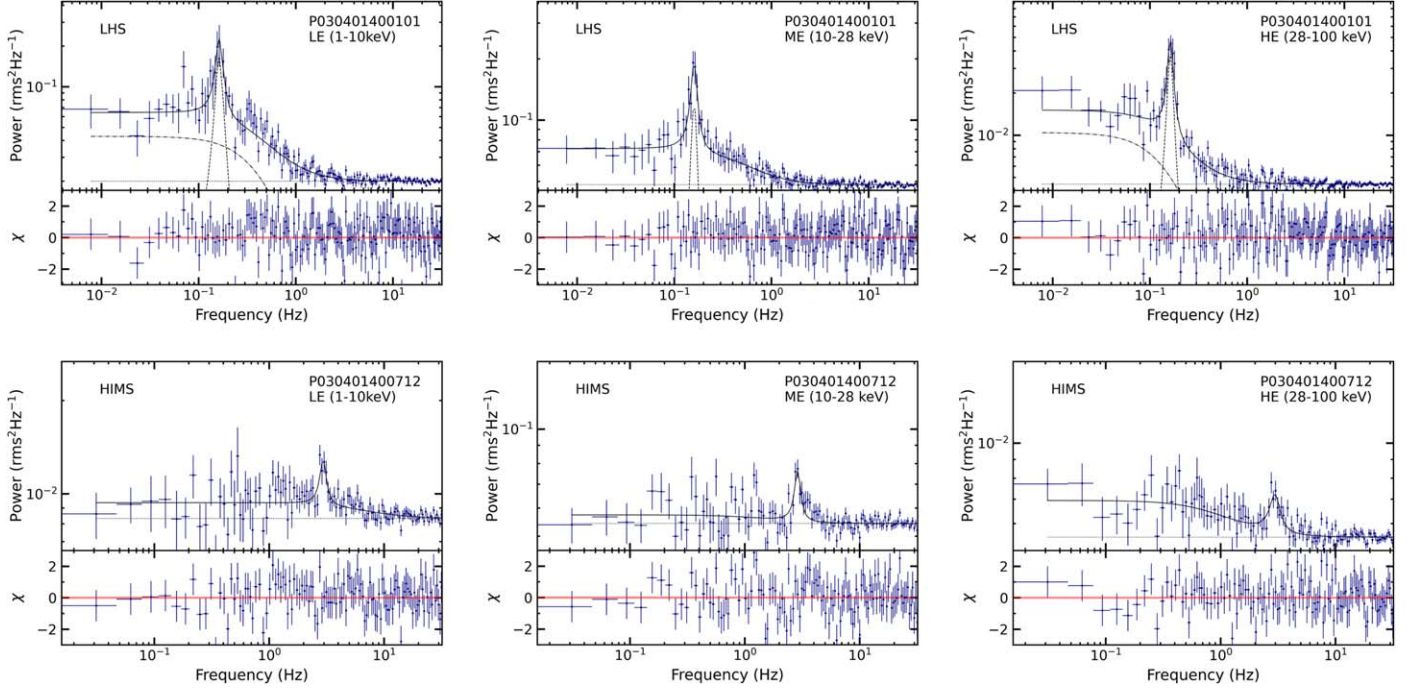
Figure 5. Six representative plots of the fitted PDS of MAXI J1803–298. ExpIDs and energy bands we used are labeled in each panel.
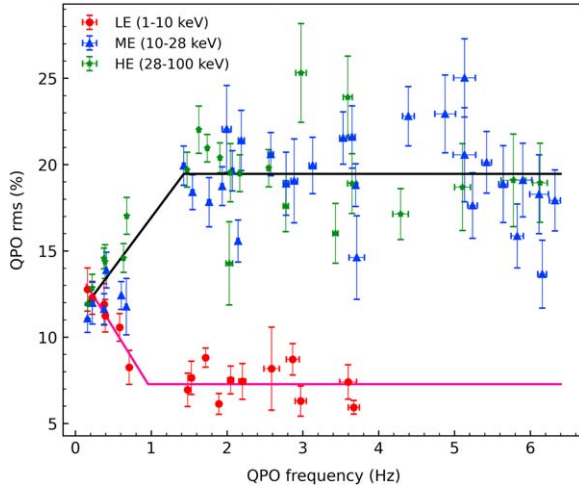

Figure 6. QPO rms of MAXI J1803–298 in three energy bands as a function of QPO frequency. Red, blue, and green points represent LE (1–10 keV), ME (10–28 keV), and HE (28–100 keV), respectively. Fitting results of the LE and the combined ME and HE with a broken line are shown in pink and black, respectively.

Figure 7. QPO lags between 10–19 keV and 1–4 keV as a function of QPO frequency for MAXI J1803–298. Black, blue and red points represent QPO lags calculated using the Insight-HXMT data, rebinned results of Insight-HXMT and the results reported by Chand et al. (2022) with AstroSat data, respectively.

phase of the outburst, the corona contracts (Kara et al. 2019), resulting in an increase in the QPO frequency. Statistical results, showing a dependency of QPO properties on the inclination angle, support this model (Motta et al. 2015; van den Eijnden et al. 2017).

In Figure 6, the QPO rms in the 1–10 keV energy band presents an opposite decreasing trend over frequency

compared to the QPO rms in the 10–28 keV and 28–100 keV band, which is consistent with the result of Zhu et al. (2023). Since the diskbb component is mainly present at energies below $\sim$10 keV, the type-C QPOs must be correlated with the Comptonized component. If the variability at the QPO frequency comes from this component, the QPO rms is given by the ratio of flux containing QPO signal

Figure 8. Eight representative plots of the fitted spectra of MAXI J1803–298 for four states. ExpIDs and the models we used are labeled in each panel.

Table 4
Best-fitting Spectral Parameters of MAXI J1803–298 Using Two Models

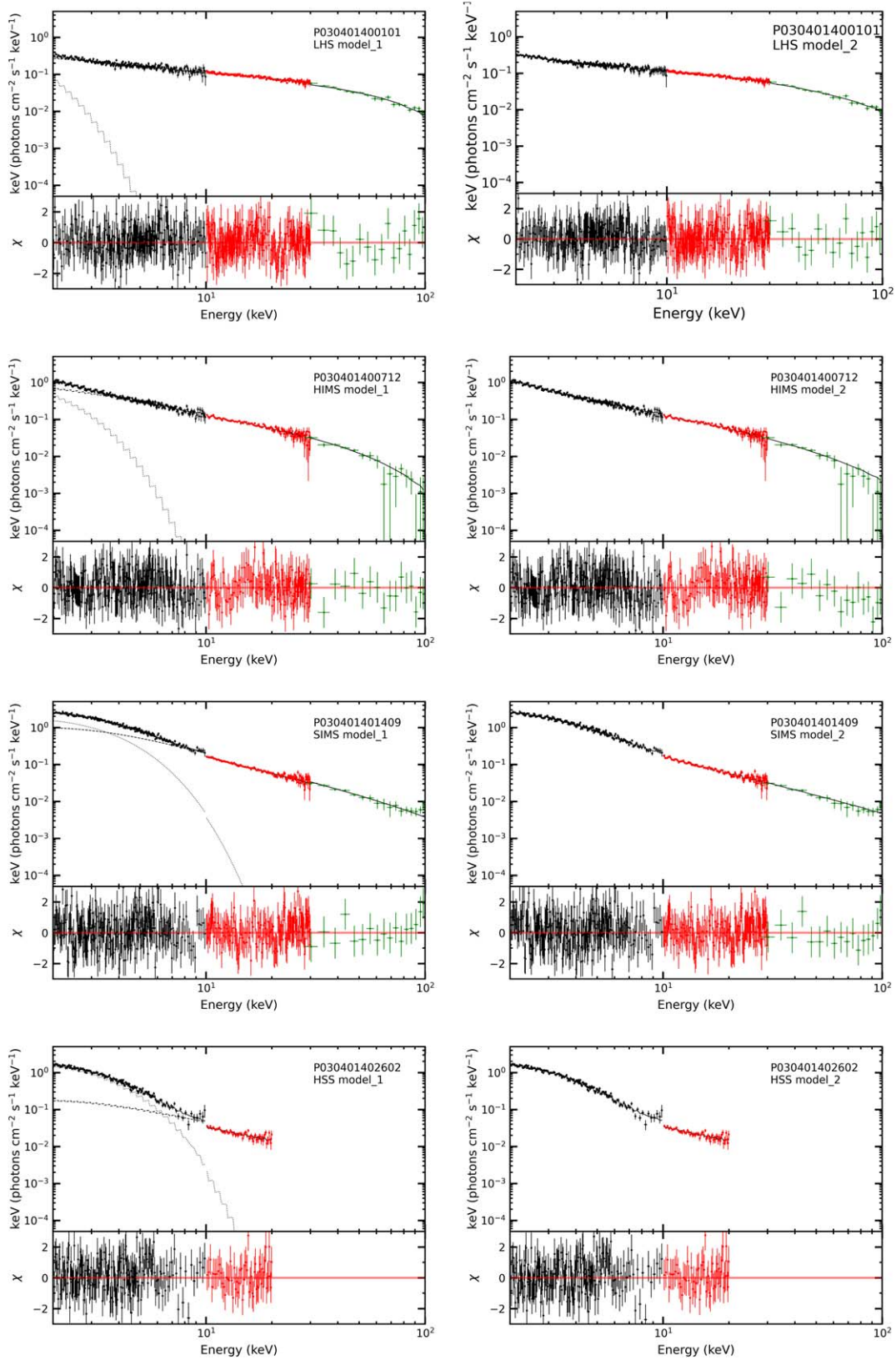| ExpID	T_{in} (keV)	N_{dbb}	Γ	kT_e (keV)	N_{nth}	Flux$_{1-100\ keV}$[a] (10^{-8} erg cm^{-2} s^{-1})	f_{dbb}[b]	χ^2/dof
				Model 1: constant $*$ TBabs $*$ (diskbb+nthcomp)				
0101	0.31 ± 0.06	12000 ± 8000	1.661 ± 0.009	19.7 ± 0.8	0.42 ± 0.03	0.848 ± 0.006	0.06 ± 0.01	684.6/991
0201	0.41 ± 0.05	2000 ± 51000	1.68 ± 0.01	16 ± 1	0.45 ± 0.03	0.877 ± 0.005	0.037 ± 0.006	756.4/1054
0301	0.27 ± 0.04	50000 ± 30000	1.68 ± 0.02	17 ± 2	0.55 ± 0.06	0.996 ± 0.005	0.08 ± 0.02	757.3/1125
0302	0.26 ± 0.03	65000 ± 3000	1.73 ± 0.02	17 ± 2	0.62 ± 0.04	0.943 ± 0.006	0.09 ± 0.04	736.1/981
0401	0.27 ± 0.02	40000 ± 10000	1.75 ± 0.02	17 ± 2	0.64 ± 0.05	0.925 ± 0.004	0.08 ± 0.02	775.7/1160
0402	0.31 ± 0.04	20000 ± 40000	1.75 ± 0.03	20 ± 90	0.6 ± 0.1	1.42 ± 0.01	0.260 ± 0.008	731.5/993
0701	0.31 ± 0.03	27000 ± 2000	1.91 ± 0.04	18 ± 2	0.95 ± 0.08	0.893 ± 0.005	0.08 ± 0.02	760.2/945
0702	0.41 ± 0.03	6000 ± 1000	1.87 ± 0.02	16 ± 5	0.80 ± 0.07	0.997 ± 0.006	0.13 ± 0.02	761.2/976
0703	0.38 ± 0.02	9500 ± 900	1.96 ± 0.03	22 ± 4	0.97 ± 0.08	0.996 ± 0.005	0.115 ± 0.009	840.8/1145
0704	0.33 ± 0.03	30000 ± 1000	1.98 ± 0.03	20 ± 10	1.1 ± 0.1	1.016 ± 0.004	0.131 ± 0.008	895.1/1085
0707	0.37 ± 0.02	12700 ± 800	1.96 ± 0.07	20 ± 970	1.0 ± 0.1	1.098 ± 0.005	0.17 ± 0.01	823.1/1031
0708	0.43 ± 0.03	5500 ± 200	2.00 ± 0.03	20 ± 11	1.03 ± 0.09	1.079 ± 0.005	0.15 ± 0.01	653.1/847
0709	0.48 ± 0.04	4000 ± 10000	1.89 ± 0.03	10 ± 20	0.8 ± 0.1	1.057 ± 0.006	0.14 ± 0.01	579.5/732
0710	0.44 ± 0.05	10000 ± 30000	2.05 ± 0.01	24.0 ± 0.9	1.12 ± 0.03	1.067 ± 0.008	0.17 ± 0.01	804.5/956
0711	0.52 ± 0.05	3000 ± 536000	2.03 ± 0.01	27 ± 1	0.95 ± 0.03	1.125 ± 0.005	0.173 ± 0.009	601.8/775
0712	0.49 ± 0.04	4000 ± 178000	2.08 ± 0.01	16 ± 3	1.07 ± 0.05	1.124 ± 0.008	0.180 ± 0.009	832.2/1028
0802	0.50 ± 0.03	4000 ± 4000	2.10 ± 0.02	23 ± 2	1.21 ± 0.04	1.060 ± 0.004	0.188 ± 0.007	618.7/786
0803	0.54 ± 0.02	3000 ± 19000	2.09 ± 0.02	22 ± 3	1.10 ± 0.06	1.261 ± 0.008	0.21 ± 0.01	691.9/862
0804	0.50 ± 0.03	4000 ± 3000	2.15 ± 0.04	42 ± 2	1.26 ± 0.08	1.277 ± 0.007	0.232 ± 0.008	591.8/678
0806	0.59 ± 0.03	2000 ± 2000	2.12 ± 0.02	200^c	1.02 ± 0.07	1.23 ± 0.01	0.20 ± 0.01	494.8/568
0807	0.52 ± 0.02	4000 ± 1200	2.20 ± 0.03	37 ± 6	1.42 ± 0.09	1.25 ± 0.01	0.20 ± 0.01	621.8/752
0810	0.66 ± 0.04	2000 ± 2000	2.31 ± 0.03	110 ± 20	1.2 ± 0.1	1.359 ± 0.009	0.22 ± 0.01	661.0/748
0901	0.73 ± 0.04	1000 ± 1000	2.24 ± 0.04	40 ± 1000	1.1 ± 0.1	1.343 ± 0.009	0.272 ± 0.008	629.6/743
0904	0.65 ± 0.03	1600 ± 300	2.28 ± 0.03	100 ± 100	1.3 ± 0.1	1.44 ± 0.01	0.296 ± 0.007	659.5/734
1012	0.99 ± 0.04	530 ± 40	2.43 ± 0.02	200^c	1.2 ± 0.1	2.14 ± 0.03	0.385 ± 0.009	612.0/715
1103	0.96 ± 0.04	660 ± 60	2.48 ± 0.04	200^c	1.0 ± 0.2	1.91 ± 0.02	0.460 ± 0.007	719.9/821
1104	0.99 ± 0.02	640 ± 40	2.44 ± 0.05	200^c	0.69 ± 0.08	1.69 ± 0.02	0.57 ± 0.01	599.9/673
1106	0.97 ± 0.03	630 ± 40	2.48 ± 0.06	200^c	1.18 ± 0.09	2.04 ± 0.04	0.42 ± 0.01	649.3/705
1110	0.99 ± 0.02	630 ± 30	2.37 ± 0.04	200^c	0.57 ± 0.06	1.61 ± 0.02	0.60 ± 0.01	629.3/739
1111	0.98 ± 0.02	650 ± 30	2.48 ± 0.04	200^c	0.58 ± 0.06	1.52 ± 0.02	0.615 ± 0.008	750.1/852
1112	1.02 ± 0.02	570 ± 50	2.35 ± 0.05	200^c	0.48 ± 0.07	1.55 ± 0.02	0.63 ± 0.01	498.0/659
1113	1.00 ± 0.03	660 ± 20	2.41 ± 0.03	200^c	0.5 ± 0.1	1.60 ± 0.02	0.66 ± 0.01	485.1/647
1201	1.01 ± 0.02	640 ± 30	2.40 ± 0.02	200^c	0.40 ± 0.07	1.51 ± 0.01	0.703 ± 0.008	610.7/780
1301	0.93 ± 0.02	730 ± 40	2.34 ± 0.03	200^c	0.7 ± 0.1	1.60 ± 0.02	0.527 ± 0.008	793.2/889
1305	0.99 ± 0.02	700 ± 300	2.35 ± 0.02	200^c	0.44 ± 0.08	1.48 ± 0.02	0.661 ± 0.009	753.3/838
1401	0.96 ± 0.03	700 ± 200	2.53 ± 0.02	200^c	0.62 ± 0.06	1.52 ± 0.01	0.613 ± 0.007	771.6/867
1402	0.92 ± 0.02	780 ± 40	2.35 ± 0.02	200^c	0.74 ± 0.08	1.65 ± 0.02	0.516 ± 0.009	721.8/821
1403	0.95 ± 0.02	690 ± 40	2.48 ± 0.02	200^c	0.72 ± 0.05	1.59 ± 0.02	0.555 ± 0.008	743.1/885
1404	0.90 ± 0.03	730 ± 50	2.48 ± 0.02	200^c	0.9 ± 0.2	1.60 ± 0.03	0.46 ± 0.01	594.6/651
1407	1.01 ± 0.04	540 ± 70	2.40 ± 0.04	200^c	0.8 ± 0.2	1.83 ± 0.02	0.490 ± 0.005	828.5/966
1408	1.01 ± 0.02	510 ± 50	2.34 ± 0.05	200^c	0.91 ± 0.09	1.96 ± 0.02	0.439 ± 0.005	834.3/977
1409	0.94 ± 0.03	640 ± 50	2.41 ± 0.06	200^c	1.2 ± 0.1	2.01 ± 0.02	0.386 ± 0.005	781.1/953
1410	0.98 ± 0.01	630 ± 40	2.19 ± 0.04	200^c	0.74 ± 0.06	1.97 ± 0.03	0.475 ± 0.008	787.2/885
1411	0.93 ± 0.01	650 ± 30	2.39 ± 0.04	200^c	1.29 ± 0.06	2.06 ± 0.03	0.354 ± 0.006	763.4/877
1601	0.64 ± 0.02	1710 ± 50	2.26 ± 0.05	200^c	1.05 ± 0.07	1.24 ± 0.01	0.284 ± 0.007	720.8/800
1701	0.60 ± 0.03	1900 ± 80	2.32 ± 0.03	200^c	1.1 ± 0.1	1.13 ± 0.01	0.257 ± 0.009	679.1/769
1702	0.68 ± 0.02	1340 ± 30	2.18 ± 0.02	200^c	0.88 ± 0.08	1.24 ± 0.02	0.292 ± 0.009	547.9/705
1703	0.69 ± 0.02	1260 ± 50	2.23 ± 0.03	200^c	1.0 ± 0.1	1.34 ± 0.01	0.280 ± 0.005	836.6/974
1801	0.89 ± 0.02	600 ± 400	2.39 ± 0.03	200^c	1.15 ± 0.09	1.73 ± 0.02	0.334 ± 0.006	789.2/894
1802	0.90 ± 0.02	600 ± 200	2.29 ± 0.02	200^c	1.00 ± 0.07	1.75 ± 0.02	0.358 ± 0.006	745.6/878
1901	0.88 ± 0.02	650 ± 50	2.31 ± 0.02	200^c	1.00 ± 0.08	1.67 ± 0.02	0.353 ± 0.005	826.6/972
2001	0.89 ± 0.02	640 ± 40	2.34 ± 0.02	200^c	0.86 ± 0.06	1.53 ± 0.01	0.403 ± 0.005	851.3/997
2101	0.84 ± 0.02	740 ± 40	2.47 ± 0.04	200^c	1.13 ± 0.08	1.53 ± 0.01	0.359 ± 0.005	682.0/776
2102	0.85 ± 0.02	700 ± 60	2.50 ± 0.06	200^c	1.03 ± 0.08	1.40 ± 0.02	0.374 ± 0.006	662.4/692
2103	0.84 ± 0.02	810 ± 60	2.5 ± 0.1	200^c	0.82 ± 0.08	1.31 ± 0.02	0.457 ± 0.009	549.8/579
2201	0.86 ± 0.01	840 ± 30	2.3 ± 0.1	200^c	0.43 ± 0.04	1.12 ± 0.02	0.61 ± 0.01	586.0/628
2202	0.84 ± 0.02	900 ± 40	2.41 ± 0.09	200^c	0.58 ± 0.05	1.18 ± 0.02	0.548 ± 0.009	653.1/619
2203	0.85 ± 0.01	880 ± 30	2.44 ± 0.09	200^c	0.55 ± 0.03	1.16 ± 0.02	0.57 ± 0.01	485.0/523
2301	0.91 ± 0.01	790 ± 30	2.21 ± 0.09	200^c	0.21 ± 0.03	1.09 ± 0.02	0.76 ± 0.01	589.0/648
2302	0.92 ± 0.01	760 ± 40	2.4 ± 0.1	200^c	0.20 ± 0.04	1.02 ± 0.01	0.80 ± 0.01	578.1/623
2303	0.91 ± 0.01	780 ± 40	2.3 ± 0.2	200^c	0.17 ± 0.07	1.01 ± 0.02	0.81 ± 0.02	503.0/523

Table 4
(Continued)

			Model 1: constant * TBabs * (diskbb+nthcomp)					
ExpID	T_{in} (keV)	N_{dbb}	Γ	kT_e (keV)	N_{nth}	Flux$_{1-100\ keV}$[a] (10^{-8} erg cm^{-2} s^{-1})	f_{dbb}[b]	χ^2/dof
2501	0.90 ± 0.01	790 ± 40	2.3 ± 0.3	200^c	0.25 ± 0.09	1.06 ± 0.02	0.74 ± 0.01	590.5/617
2502	0.91 ± 0.02	780 ± 60	2.19 ± 0.06	200^c	0.20 ± 0.09	1.07 ± 0.02	0.75 ± 0.01	567.0/639
2601	0.89 ± 0.01	780 ± 60	2.23 ± 0.07	200^c	0.23 ± 0.07	1.00 ± 0.02	0.72 ± 0.01	603.7/663
2602	0.89 ± 0.02	770 ± 70	2.1 ± 0.1	200^c	0.21 ± 0.09	1.00 ± 0.02	0.71 ± 0.01	607.4/645
2702	0.88 ± 0.02	840 ± 50	2.3 ± 0.2	200^c	0.26 ± 0.06	1.02 ± 0.01	0.73 ± 0.01	627.7/671
2703	0.89 ± 0.01	810 ± 40	2.32 ± 0.09	200^c	0.20 ± 0.04	0.97 ± 0.02	0.78 ± 0.01	622.3/629
2802	0.87 ± 0.01	870 ± 30	2.1 ± 0.1	200^c	0.15 ± 0.03	0.99 ± 0.02	0.77 ± 0.02	571.6/599
2803	0.89 ± 0.01	800 ± 40	2.0 ± 0.1	200^c	0.12 ± 0.05	0.94 ± 0.03	0.80 ± 0.02	534.7/557
2901	0.86 ± 0.01	860 ± 40	2.8 ± 0.2	200^c	0.28 ± 0.04	0.88 ± 0.01	0.79 ± 0.01	503.8/619
3001	0.84 ± 0.01	830 ± 40	3.1 ± 0.3	200^c	0.3 ± 0.1	0.808 ± 0.008	0.764 ± 0.009	540.6/639
3101	0.79 ± 0.05	800 ± 500	4 ± 1	200^c	0.9 ± 0.6	0.800 ± 0.007	0.559 ± 0.008	410.3/470
3201	0.79 ± 0.02	900 ± 700	4.2 ± 0.8	200^c	0 ± 1	0.774 ± 0.007	0.600 ± 0.008	425.1/464
3301	0.72 ± 0.01	1 ± 73	5 ± 1	200^c	2 ± 1	0.747 ± 0.006	0 ± 133835091	443.1/498
3401	0.70 ± 0.03	0 ± 100	5 ± 1	200^c	2 ± 1	0.739 ± 0.007	0 ± 135328728	419.7/590
3601	0.70 ± 0.01	0 ± 1000	5.4 ± 0.2	200^c	2.36 ± 0.05	0.683 ± 0.007	0.21 ± 0.01	385.8/492
3701	0.71 ± 0.02	100 ± 600	5.5 ± 0.3	200^c	2.12 ± 0.15	0.650 ± 0.006	0.04 ± 0.02	439.3/551

			Model 2: constant * TBabs * (simplcutx * diskbb)					
ExpID	T_{in} (keV)	N_{dbb}	Γ	E_{cut} (keV)	f_{sc}	Flux$_{1-100\ keV}$ (10^{-8} erg cm^{-2} s^{-1})	f_{dbb}	χ^2/dof
0101	0.54 ± 0.02	1100 ± 200	1.28 ± 0.03	48 ± 4	0.42 ± 0.01	0.853 ± 0.005	0.118 ± 0.002	727.6/1050
0201	0.58 ± 0.03	1000 ± 300	1.21 ± 0.05	37 ± 4	0.40 ± 0.02	0.919 ± 0.005	0.133 ± 0.002	782.0/1113
0301	0.51 ± 0.02	1900 ± 400	1.28 ± 0.05	41 ± 4	0.39 ± 0.02	0.984 ± 0.004	0.122 ± 0.002	797.7/1184
0302	0.50 ± 0.01	2000 ± 1000	1.39 ± 0.04	43 ± 6	0.43 ± 0.01	0.895 ± 0.005	0.134 ± 0.002	801.4/1040
0401	0.46 ± 0.01	3100 ± 700	1.43 ± 0.04	46 ± 6	0.40 ± 0.01	0.923 ± 0.004	0.130 ± 0.002	815.5/1219
0402	0.48 ± 0.01	2600 ± 800	1.40 ± 0.04	39 ± 7	0.38 ± 0.02	0.876 ± 0.005	0.148 ± 0.003	772.7/1052
0701	0.41 ± 0.02	9000 ± 900	1.65 ± 0.09	45 ± 8	0.32 ± 0.03	0.984 ± 0.005	0.201 ± 0.003	792.4/1004
0702	0.45 ± 0.02	6000 ± 800	1.62 ± 0.05	50 ± 20	0.32 ± 0.02	1.023 ± 0.004	0.214 ± 0.003	824.1/1035
0703	0.45 ± 0.01	6700 ± 400	1.75 ± 0.07	50 ± 20	0.36 ± 0.02	1.002 ± 0.003	0.232 ± 0.002	885.8/1204
0704	0.45 ± 0.02	7100 ± 700	1.75 ± 0.05	50 ± 500	0.35 ± 0.03	1.031 ± 0.004	0.245 ± 0.003	970.7/1144
0707	0.46 ± 0.01	6500 ± 400	1.73 ± 0.06	50 ± 80	0.34 ± 0.03	1.053 ± 0.004	0.244 ± 0.003	863.5/1090
0708	0.47 ± 0.02	6600 ± 300	1.78 ± 0.06	50 ± 40	0.34 ± 0.02	1.071 ± 0.005	0.267 ± 0.004	701.4/906
0709	0.49 ± 0.02	5400 ± 200	1.71 ± 0.03	47 ± 3	0.33 ± 0.02	1.128 ± 0.007	0.268 ± 0.005	640.5/791
0710	0.49 ± 0.02	5900 ± 400	1.87 ± 0.04	56 ± 4	0.35 ± 0.02	1.118 ± 0.004	0.306 ± 0.003	855.6/1015
0711	0.50 ± 0.02	6000 ± 500	1.92 ± 0.04	80 ± 4	0.36 ± 0.02	1.152 ± 0.006	0.307 ± 0.004	684.8/834
0712	0.50 ± 0.01	6000 ± 2000	1.92 ± 0.04	48 ± 5	0.36 ± 0.02	1.073 ± 0.004	0.334 ± 0.003	886.9/1087
0802	0.56 ± 0.01	4300 ± 800	1.88 ± 0.04	47 ± 5	0.33 ± 0.01	1.246 ± 0.007	0.369 ± 0.005	687.6/845
0803	0.57 ± 0.01	4000 ± 1000	1.96 ± 0.04	64 ± 6	0.35 ± 0.02	1.277 ± 0.006	0.380 ± 0.004	768.6/921
0804	0.55 ± 0.02	4000 ± 1000	2.04 ± 0.09	80 ± 10	0.39 ± 0.03	1.211 ± 0.008	0.361 ± 0.006	656.3/737
0806	0.54 ± 0.02	4800 ± 900	2.13 ± 0.05	500 ± 6	0.42 ± 0.02	1.28 ± 0.01	0.335 ± 0.007	532.5/625
0807	0.58 ± 0.01	4200 ± 500	2.07 ± 0.07	70 ± 10	0.38 ± 0.03	1.326 ± 0.007	0.403 ± 0.005	697.4/811
0810	0.64 ± 0.02	3000 ± 1000	2.26 ± 0.06	100 ± 300	0.41 ± 0.04	1.360 ± 0.007	0.466 ± 0.005	715.2/807
0901	0.70 ± 0.01	2200 ± 500	2.18 ± 0.06	90 ± 40	0.38 ± 0.03	1.460 ± 0.008	0.483 ± 0.005	703.9/802
0904	0.64 ± 0.02	3200 ± 400	2.22 ± 0.05	110 ± 20	0.41 ± 0.03	1.441 ± 0.008	0.453 ± 0.005	729.7/793
1012	0.96 ± 0.02	970 ± 90	2.50 ± 0.03	500 ± 6	0.43 ± 0.04	2.16 ± 0.01	0.610 ± 0.006	648.3/774
1103	0.96 ± 0.02	950 ± 90	2.54 ± 0.04	500^c	0.33 ± 0.04	1.913 ± 0.009	0.670 ± 0.005	768.7/880
1104	0.96 ± 0.02	940 ± 50	2.52 ± 0.05	500^c	0.26 ± 0.02	1.73 ± 0.01	0.713 ± 0.008	676.5/732
1106	0.96 ± 0.02	980 ± 60	2.55 ± 0.06	500^c	0.37 ± 0.03	2.04 ± 0.01	0.646 ± 0.007	683.2/764
1110	0.98 ± 0.01	830 ± 40	2.44 ± 0.05	500^c	0.21 ± 0.02	1.622 ± 0.009	0.734 ± 0.007	672.2/798
1111	0.96 ± 0.01	870 ± 40	2.56 ± 0.05	500^c	0.22 ± 0.02	1.540 ± 0.006	0.756 ± 0.005	811.6/911
1112	0.97 ± 0.01	840 ± 40	2.46 ± 0.05	500^c	0.22 ± 0.02	1.59 ± 0.02	0.734 ± 0.008	549.2/718
1113	1.00 ± 0.02	810 ± 90	2.48 ± 0.03	500^c	0.17 ± 0.03	1.60 ± 0.01	0.793 ± 0.008	534.9/706
1201	0.98 ± 0.01	840 ± 40	2.50 ± 0.02	500^c	0.16 ± 0.02	1.536 ± 0.007	0.796 ± 0.006	677.1/839
1301	0.94 ± 0.02	930 ± 50	2.38 ± 0.03	500^c	0.24 ± 0.02	1.597 ± 0.006	0.691 ± 0.004	848.5/948
1305	0.97 ± 0.01	800 ± 300	2.42 ± 0.03	500^c	0.17 ± 0.02	1.505 ± 0.006	0.769 ± 0.005	810.5/897
1401	0.97 ± 0.02	800 ± 200	2.59 ± 0.03	500^c	0.21 ± 0.02	1.515 ± 0.006	0.774 ± 0.005	819.8/926
1402	0.92 ± 0.01	1020 ± 80	2.39 ± 0.03	500^c	0.25 ± 0.02	1.654 ± 0.007	0.681 ± 0.005	775.6/880
1403	0.94 ± 0.01	960 ± 50	2.54 ± 0.02	500^c	0.26 ± 0.01	1.612 ± 0.006	0.721 ± 0.004	811.1/944
1404	0.89 ± 0.03	1100 ± 90	2.54 ± 0.03	500^c	0.33 ± 0.03	1.60 ± 0.01	0.659 ± 0.008	635.5/710
1407	1.00 ± 0.02	800 ± 100	2.46 ± 0.04	500^c	0.30 ± 0.04	1.850 ± 0.006	0.670 ± 0.003	872.5/1025

Table 4
(Continued)

ExpID	T_{in} (keV)	N_{dbb}	Γ	kT_e (keV)	N_{nth}	Flux$_{1-100\ keV}$[a] (10^{-8} erg cm^{-2} s^{-1})	f_{dbb}[b]	χ^2/dof
			Model 1: constant ∗ TBabs ∗ (diskbb+nthcomp)					
1408	1.01 ± 0.02	750 ± 60	2.39 ± 0.05	500[c]	0.33 ± 0.02	1.973 ± 0.006	0.632 ± 0.003	898.1/1036
1409	0.96 ± 0.02	940 ± 70	2.46 ± 0.06	500[c]	0.37 ± 0.03	2.000 ± 0.006	0.617 ± 0.003	837.7/1012
1410	0.98 ± 0.01	860 ± 40	2.22 ± 0.05	500[c]	0.26 ± 0.02	1.978 ± 0.007	0.626 ± 0.004	861.2/944
1411	0.97 ± 0.01	880 ± 40	2.43 ± 0.05	500[c]	0.38 ± 0.02	2.035 ± 0.008	0.603 ± 0.004	813.2/936
1601	0.65 ± 0.01	2670 ± 40	2.30 ± 0.05	500[c]	0.40 ± 0.02	1.228 ± 0.006	0.468 ± 0.004	796.8/859
1701	0.60 ± 0.02	3200 ± 100	2.36 ± 0.03	500[c]	0.45 ± 0.03	1.124 ± 0.006	0.450 ± 0.005	726.8/828
1702	0.68 ± 0.01	2060 ± 40	2.21 ± 0.02	500[c]	0.38 ± 0.02	1.281 ± 0.008	0.442 ± 0.005	621.0/764
1703	0.69 ± 0.02	2130 ± 60	2.26 ± 0.03	500[c]	0.41 ± 0.02	1.350 ± 0.004	0.460 ± 0.003	885.1/1033
1801	0.86 ± 0.01	1200 ± 300	2.45 ± 0.03	500[c]	0.45 ± 0.02	1.753 ± 0.007	0.552 ± 0.004	848.0/953
1802	0.86 ± 0.02	1200 ± 200	2.35 ± 0.03	500[c]	0.40 ± 0.02	1.787 ± 0.007	0.543 ± 0.004	809.5/937
1901	0.86 ± 0.02	1130 ± 80	2.36 ± 0.02	500[c]	0.40 ± 0.02	1.687 ± 0.005	0.551 ± 0.003	867.3/1031
2001	0.88 ± 0.01	1040 ± 60	2.39 ± 0.02	500[c]	0.35 ± 0.01	1.546 ± 0.004	0.592 ± 0.003	919.2/1056
2101	0.85 ± 0.01	1170 ± 60	2.50 ± 0.04	500[c]	0.40 ± 0.02	1.529 ± 0.004	0.596 ± 0.004	743.4/835
2102	0.85 ± 0.01	1130 ± 70	2.54 ± 0.07	500[c]	0.40 ± 0.03	1.411 ± 0.005	0.608 ± 0.005	709.8/751
2103	0.84 ± 0.01	1180 ± 60	2.5 ± 0.1	500[c]	0.31 ± 0.03	1.314 ± 0.006	0.652 ± 0.007	608.0/638
2201	0.857 ± 0.009	1040 ± 30	2.4 ± 0.1	500[c]	0.18 ± 0.01	1.133 ± 0.004	0.735 ± 0.006	645.9/687
2202	0.84 ± 0.01	1150 ± 40	2.4 ± 0.2	500[c]	0.23 ± 0.02	1.186 ± 0.005	0.702 ± 0.006	710.7/678
2203	0.859 ± 0.008	1040 ± 30	2.5 ± 0.1	500[c]	0.21 ± 0.01	1.156 ± 0.006	0.728 ± 0.008	545.3/582
2301	0.905 ± 0.008	890 ± 30	2.2 ± 0.1	500[c]	0.09 ± 0.01	1.099 ± 0.004	0.825 ± 0.006	646.5/707
2302	0.910 ± 0.008	850 ± 30	2.4 ± 0.2	500[c]	0.09 ± 0.02	1.028 ± 0.004	0.862 ± 0.006	646.6/682
2303	0.908 ± 0.009	850 ± 40	2.3 ± 0.2	500[c]	0.07 ± 0.03	1.011 ± 0.005	0.870 ± 0.009	546.2/582
2501	0.90 ± 0.01	870 ± 60	2.3 ± 0.3	500[c]	0.10 ± 0.04	1.064 ± 0.004	0.827 ± 0.006	643.6/676
2502	0.90 ± 0.01	880 ± 80	2.21 ± 0.06	500[c]	0.09 ± 0.03	1.080 ± 0.004	0.818 ± 0.006	641.2/698
2601	0.89 ± 0.01	870 ± 60	2.24 ± 0.07	500[c]	0.10 ± 0.02	1.009 ± 0.003	0.803 ± 0.005	668.5/722
2602	0.88 ± 0.01	910 ± 70	2.2 ± 0.1	500[c]	0.10 ± 0.03	1.015 ± 0.004	0.778 ± 0.006	672.2/704
2702	0.87 ± 0.01	960 ± 40	2.4 ± 0.2	500[c]	0.11 ± 0.02	1.025 ± 0.003	0.815 ± 0.005	699.3/730
2703	0.879 ± 0.008	920 ± 30	2.4 ± 0.1	500[c]	0.09 ± 0.01	0.973 ± 0.004	0.843 ± 0.006	679.8/688
2802	0.881 ± 0.008	900 ± 30	2.0 ± 0.1	500[c]	0.06 ± 0.01	0.988 ± 0.004	0.824 ± 0.006	643.7/658
2803	0.879 ± 0.008	890 ± 40	2.1 ± 0.2	500[c]	0.06 ± 0.02	0.949 ± 0.004	0.834 ± 0.007	578.2/616
2901	0.859 ± 0.009	970 ± 40	2.9 ± 0.2	500[c]	0.12 ± 0.01	0.885 ± 0.003	0.888 ± 0.007	556.0/678
3001	0.833 ± 0.009	1030 ± 50	3.2 ± 0.3	500[c]	0.16 ± 0.05	0.814 ± 0.003	0.885 ± 0.007	604.8/698
3101	0.84 ± 0.02	980 ± 60	3 ± 2	500[c]	0.09 ± 0.05	0.824 ± 0.003	0.811 ± 0.006	468.4/529
3201	0.85 ± 0.01	950 ± 70	1 ± 1	500[c]	0.0 ± 0.1	0.842 ± 0.003	0.851 ± 0.008	493.4/523
3301	0.81 ± 0.01	1100 ± 100	3 ± 1	500[c]	0.2 ± 0.1	0.739 ± 0.002	0.859 ± 0.006	495.8/557
3401	0.81 ± 0.01	1050 ± 70	3 ± 1	500[c]	0.2 ± 0.1	0.735 ± 0.002	0.823 ± 0.006	496.9/649
3601	0.77 ± 0.02	1230 ± 90	4 ± 1	500[c]	0.5 ± 0.2	0.671 ± 0.002	0.852 ± 0.007	447.3/551
3701	0.78 ± 0.02	1100 ± 100	4 ± 1	500[c]	0.3 ± 0.1	0.647 ± 0.002	0.845 ± 0.006	506.9/610

Notes.
[a] Unabsorbed total flux calculated in 1–100 keV.
[b] The ratio of disk flux to total flux.
[c] During the SIMS and the HSS, kT_e and E_{cut} are fixed at 200 keV and 500 keV, respectively.

to the total flux. Zhu et al. (2023) and Chand et al. (2022) studied the QPO rms spectra, which are similar to the results of previous studies from other sources, like XTE J1859+226, H 1743–322 and MAXI J1535–571 (Casella et al. 2004; Li et al. 2013; Kong et al. 2020), consistent with the simulation results of You et al. (2018) utilizing a model incorporating LT precession of the inner flow. We present the QPO phase lags where the QPO was detected over the frequency range from ∼1.6 to 6.1 Hz in Figure 7. Significant hard lags are detected for QPO frequency less than ∼2 Hz, with a trend shifting toward soft lags. Meanwhile, Chand et al. (2022) reported soft lags at ∼6 Hz. Such results are consistent with

the statistical results of high-inclination sources (van den Eijnden et al. 2017). van den Eijnden et al. (2017) elucidated the inclination dependence of the type-C QPO phase lag via the work of Veledina et al. (2013) modeling precessing rings, that is, the opposite sign of the lag between low- and high-inclination systems mainly due to the trade-off between the Doppler effect and the solid angle effect on the flux modulation.

Moreover, the time-dependent Comptonization model, which considers coupled oscillations of the physical quantities, can also explain the observed QPO rms and QPO phase lags properties (Karpouzas et al. 2020; Bellavita et al. 2022). In this
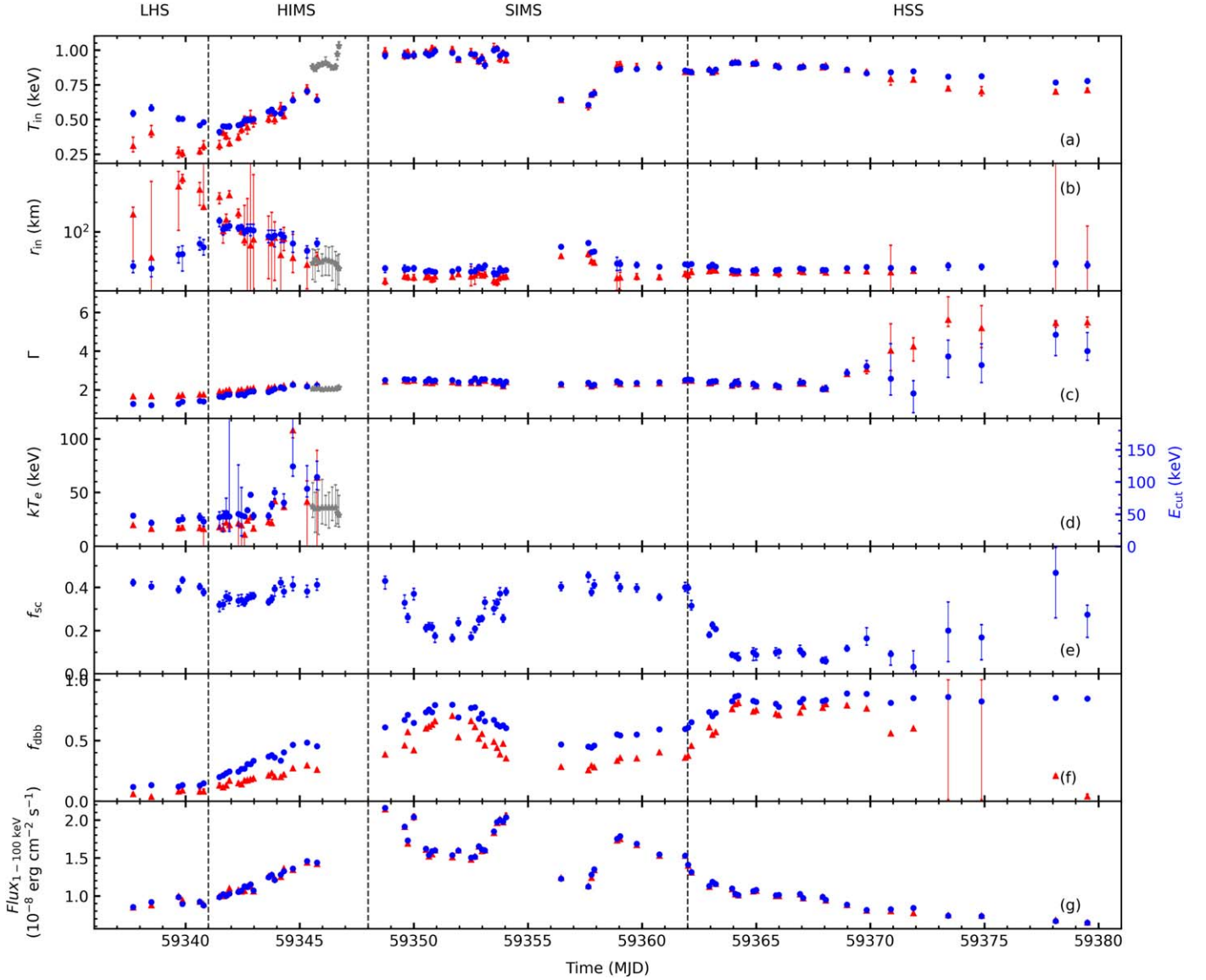
Figure 9. Best-fitting spectral parameters of MAXI J1803–298: (a) temperature at r_{in} (keV); (b) r_{in} (km) calculated assuming a distance to the source $d = 8$ kpc and an inclination angle $i = 70°$; (c) power-law photon index; (d) electron temperature or exponential cutoff energy (keV); (e) scattered portion of disk photons by the corona; (f) diskbb component flux fraction in the 1–100 keV band; (g) unabsorbed bolometric flux in the 1–100 keV band. The red and blue points represent model 1 and model 2, respectively. Gray points represent the spectral results from Jana et al. (2022). The vertical lines signify the moment of the state transitions.

model, the QPO dynamical mechanism is not specified, and it can be LT precession or others. Mastichiadis et al. (2022) proposed that the QPO frequency is generated from the interactions of hot electrons and soft disk photons, within the same essence of the time-dependent Comptonization model. Sign shift in QPO lags can be interpreted as due to involving the feedback onto the disk (Karpouzas et al. 2020; Bellavita et al. 2022). Méndez et al. (2022) analyzed Rossi X-ray Timing Explorer data of GRS 1915+105, and proposed that the corona evolves to a radio jet as the QPO frequency decreases from ~6 Hz to ≲2 Hz. Correspondingly, the QPO phase lag shifts

from a soft lag to a hard lag due to the decrease of the feedback fraction.

4.2. Spectral Evolution and State Transition

In our energy spectra analysis (Section 3.3), we employed both model 1 and model 2. The residuals of the spectral data (Figure 8) show only a faint iron line component remaining. However, Xu & Harrison (2021) and Chand et al. (2022) reported the presence of reflection features, an iron line at 6–7 keV and a reflection hump at 20–30 keV, which are not prominent in the HXMT data. One reason for this disparity is the limited exposure time, while another
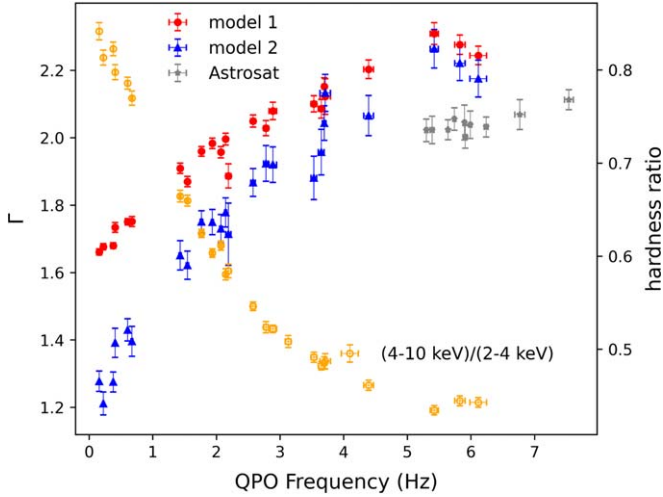
Figure 10. Hardness ratio and parameter Γ as functions of QPO frequency. Red and blue dots represent the parameter Γ obtained through model 1 and model 2 respectively. Gray dots represent the parameter Γ reported by Jana et al. (2022). Orange dots represent the hardness ratio for LE.

factor is the relatively small effective area[11] in the energy band associated with the reflection component.

Insight-HXMT commenced observations of MAXI J1803–298 at the beginning of its outburst and detected the source in the LHS, in which the source exhibited a hard spectrum dominated by a Comptonized component ($\Gamma \sim 1.3$ and $f_{\rm dbb} \sim 0.12$). However, contrary to the predictions of the truncated disk model, the inner disk radius appeared to be moving away from the black hole before MJD 59341, as illustrated in Figure 9. Previous works introduced the color-correction factor $f_{\rm col}$, a coefficient of $T_{\rm in}$ relative to the theoretically predicted effective temperature ($T_{\rm eff}$), to explain the abnormally increasing $r_{\rm in}$ obtained from a continuous spectral fitting in LHS (Merloni et al. 2000; Dunn et al. 2011; Ren et al. 2022). The $f_{\rm col} \sim (\kappa_{\rm es}^*/\kappa_{\rm th}^*)^{1/8} \propto \rho_*^{-1/8} T_*^{7/16}$, where $\kappa_{\rm es}^*$, $\kappa_{\rm th}^*$, ρ_* and T_* represent electron scattering opacity, absorption opacity, gas density at the effective photosphere and gas temperature, respectively (Salvesen & Miller 2021). If we consider that the disk was truncated and approaching the black hole during the early outburst, this would result in a decreasing trend of $f_{\rm col}$, implying an increase in gas density during this period. It may be due to the optically thick disk being condensed by the optically thin corona (Taam et al. 2008; Liu et al. 2011; Zhang et al. 2022). During this period, the gas density of the disk is not in equilibrium, and as the density increases, the $f_{\rm col}$ decreases, causing the trend of $r_{\rm in}$ we obtained.

We suggest that a transition between the LHS and the HIMS occurred around MJD 59341; this is supported by several pieces of evidence. First, prior to this time, the count rate and total fractional rms exhibited rapid variations alongside a subtle

hardness ratio change, which aligns with the LHS branch in the classical HID and HRD (Cabanac et al. 2010). During this period, the total fractional rms exceeded 20%. Second, QPO rms exhibited different trends with QPO frequency at a turning point of ~ 1 Hz, corresponding to MJD 59341. Moreover, after this time, both the photon index Γ and the parameter $f_{\rm dbb}$ exceeded the values of 1.7% and 20%, respectively. Furthermore, $r_{\rm in}$ then presented a decreasing trend, consistent with the truncated disk model and the trend of the type-C QPO frequency we observed. Type-C QPOs appeared in both LHS and HIMS, and the latest QPO was detected by Jana et al. (2022) around MJD 59346.7.

MJD $59348.08^{+0.05}_{-0.06}$ is an ejection date inferred by Wood et al. (2023). The parameters $T_{\rm in}$, $r_{\rm in}$ and Γ remained relatively constant after this point. The total fractional rms also decreased to a low value of less than 10%. We suggest that the source entered the SIMS around this time. In addition, NICER detected type-B QPOs between MJD 59352 and MJD 59358, which further confirms that the source was in the SIMS. It seems that the disk reached the $R_{\rm ISCO}$ during the SIMS, with an averaged value of 45 ± 6 km.

We observe two anomalous changes in the spectral parameters during the SIMS: a decrease in $f_{\rm sc}$ from MJD 59348 to MJD 59354 and a decrease in $T_{\rm in}$ (with an increase in $r_{\rm in}$, $f_{\rm sc}$ and total fractional rms) around MJD 59357. These changes coincided with two significant drops in the light curve. Regarding the first flux drop, where only $f_{\rm sc}$ significantly decreased, this suggests a decrease of optical depth τ or that the corona received a smaller proportion of disk radiation despite no apparent change in the disk component. An observation of NuSTAR on MJD 59349 was analyzed by Coughenour et al. (2023), and the spectra were successfully fitted with reflection models of both a lamppost geometry and a broken-power law disk emissivity. Due to data limitations, we cannot rule out the influence of the jet, and prefer the corona to be a jet-like corona extended vertically (You et al. 2021; Ma et al. 2024). For the second flux drop, Shidatsu et al. (2022) made a detailed analysis using MAXI/GSC (2–20 keV) and Swift/BAT (20–100 keV). They found that the luminosity exceeded $L_{\rm Edd}$ before decreasing, and that the disk may be a slim rather than a standard disk. It is probable that the rapidly increasing mass accretion rate caused a geometrically thicker inner disk, which reduced the apparent flux.

After MJD 59362, $f_{\rm sc}$ began to decline, reaching a low value of ~ 0.1. Simultaneously, $f_{\rm dbb}$ increased up to a high value of ~ 0.8, marking the source transition to the HSS. These changes in the spectral parameters indicate that the scale of the corona was reaching a minimum value.

5. Conclusion

We have analyzed a complete evolution of the 2021 outburst of the BHXB MAXI J1803–298 from the LHS to the HSS with the Insight-HXMT data. The main results are:

(a) The QPO frequency increased gradually with time, from the initial 0.16 Hz to around 6.3 Hz, and then decreased to 5.1 Hz, exhibiting correlations with hardness ratio and energy spectrum parameter Γ.

(b) The QPO rms in the 1–10 keV energy band decreases over time for QPO frequencies $\lesssim 1$ Hz. Beyond this frequency, the QPO rms remains more or less constant. The QPO rms in the 10–28 keV and 28–100 keV presents the opposite trend to 1–10 keV. The QPO phase lags are hard when the QPO frequency $\lesssim 2$ Hz, shifting to soft lags at and above ~ 4 Hz.

(c) We propose that for MAXI J1803–298, the transitions occurred as follows: from LHS to HIMS around MJD 59341, from HIMS to SIMS around MJD 59341, and from SIMS to HSS around MJD 59362.

(d) We obtain an abnormal trend of r_{in} during the LHS, and consider a condensing inner disk from the corona to explain it. There are two large-scale drops of flux during SIMS, maybe corresponding to the evolution in the corona/jet and disk, respectively.

ORCID iDs

Yue Huang ⓘ https://orcid.org/0000-0002-3515-9500
Li-Ming Song ⓘ https://orcid.org/0000-0003-0274-3396

References

Bellavita, C., García, F., Méndez, M., & Karpouzas, K. 2022, MNRAS, 515, 2099
Belloni, T., & Hasinger, G. 1990, A&A, 230, 103
Belloni, T. M., & Motta, S. E. 2016, in Astrophysics of Black Holes: From Fundamental Aspects to Latest Developments, ed. C. Bambi (Berlin: Springer), 61
Bult, P. M., Gendreau, K. C., Enoto, T., et al. 2021, ATel, 14602, 1
Cabanac, C., Henri, G., Petrucci, P. O., et al. 2010, MNRAS, 404, 738
Cao, X., Jiang, W., Meng, B., et al. 2020, SCPMA, 63, 249504
Casella, P., Belloni, T., Homan, J., & Stella, L. 2004, A&A, 426, 587
Casella, P., Belloni, T., & Stella, L. 2005, ApJ, 629, 403
Chand, S., Dewangan, G. C., Thakur, P., Tripathi, P., & Agrawal, V. K. 2022, ApJ, 933, 69
Chen, Y., Cui, W., Li, W., et al. 2020, SCPMA, 63, 249505
Coughenour, B. M., Tomsick, J. A., Mastroserio, G., et al. 2023, ApJ, 949, 70
Done, C., Gierliński, M., & Kubota, A. 2007, A&ARv, 15, 1
Dunn, R. J. H., Fender, R. P., Körding, E. G., Belloni, T., & Merloni, A. 2011, MNRAS, 411, 337
Esin, A. A., McClintock, J. E., & Narayan, R. 1997, ApJ, 489, 865
Fender, R. P., Belloni, T. M., & Gallo, E. 2004, MNRAS, 355, 1105
Feng, Y., Zhao, X., Li, Y., et al. 2022, MNRAS, 516, 2074
Frank, J., King, A. R., & Lasota, J. P. 1987, A&A, 178, 137
Guo, C. C., Liao, J.-Y., Zhang, S., et al. 2020, JHEAp, 27, 44
Hasinger, G., & van der Klis, M. 1989, A&A, 225, 79
Homan, J., Gendreau, K. C., Sanna, A., et al. 2021, ATel, 14606, 1
Ingram, A., Done, C., & Fragile, P. C. 2009, MNRAS, 397, L101
Ingram, A. R., & Motta, S. E. 2019, NewAR, 85, 101524
Jana, A., Naik, S., Jaisawal, G. K., et al. 2022, MNRAS, 511, 3922
Kara, E., Steiner, J. F., Fabian, A. C., et al. 2019, Natur, 565, 198
Karpouzas, K., Méndez, M., Ribeiro, E. M., et al. 2020, MNRAS, 492, 1399
Kong, L. D., Zhang, S., Chen, Y. P., et al. 2020, JHEAp, 25, 29
Li, Z. B., Zhang, S., Qu, J. L., et al. 2013, MNRAS, 433, 412
Liao, J. Y., Zhang, S., Chen, Y., et al. 2020, JHEAp, 27, 24
Liu, B. F., Done, C., & Taam, R. E. 2011, ApJ, 726, 10
Liu, C., Zhang, Y., Li, X., et al. 2020, SCPMA, 63, 249503
Ma, R., Tao, L., Méndez, M., et al. 2024, MNRAS, 528, 3864
Ma, X., Tao, L., Zhang, S.-N., et al. 2021, NatAs, 5, 94
Mastichiadis, A., Petropoulou, M., & Kylafis, N. D. 2022, A&A, 662, A118
McClintock, J. E., & Remillard, R. A. 2006, Compact Stellar X-ray Sources, Vol. 39 (Cambridge: Cambridge University Press), 157
Méndez, M., Karpouzas, K., García, F., et al. 2022, NatAs, 6, 577
Merloni, A., Fabian, A. C., & Ross, R. R. 2000, MNRAS, 313, 193
Motta, S., Belloni, T., & Homan, J. 2009, MNRAS, 400, 1603
Motta, S. E., Casella, P., Henze, M., et al. 2015, MNRAS, 447, 2059
Remillard, R. A., & McClintock, J. E. 2006, ARA&A, 44, 49
Ren, X. Q., Wang, Y., Zhang, S. N., et al. 2022, ApJ, 932, 66
Salvesen, G., & Miller, J. M. 2021, MNRAS, 500, 3640
Serino, M., Negoro, H., Nakajima, M., et al. 2021, ATel, 14587, 1
Shidatsu, M., Kobayashi, K., Negoro, H., et al. 2022, ApJ, 927, 151
Stiele, H., Belloni, T. M., Kalemci, E., & Motta, S. 2013, MNRAS, 429, 2655
Taam, R. E., Liu, B. F., Meyer, F., & Meyer-Hofmeister, E. 2008, ApJ, 688, 527
Tagger, M., & Pellat, R. 1999, A&A, 349, 1003
Tetarenko, B. E., Sivakoff, G. R., Heinke, C. O., & Gladstone, J. C. 2016, ApJS, 222, 15
Titarchuk, L., & Fiorito, R. 2004, ApJ, 612, 988
Ubach, S., Steiner, J., Homan, J., et al. 2021, ATel, 14660, 1
van den Eijnden, J., Ingram, A., Uttley, P., et al. 2017, MNRAS, 464, 2643
van der Klis, M. 2004, arXiv:astro-ph/0410551
Vaughan, B. A., & Nowak, M. A. 1997, ApJL, 474, L43
Veledina, A., Poutanen, J., & Ingram, A. 2013, ApJ, 778, 165
Verner, D. A., Ferland, G. J., Korista, K. T., & Yakovlev, D. G. 1996, ApJ, 465, 487
Wilms, J., Allen, A., & McCray, R. 2000, ApJ, 542, 914
Wood, C. M., Miller-Jones, J. C. A., Bahramian, A., et al. 2023, MNRAS, 522, 70
Xu, Y., & Harrison, F. 2021, ATel, 14609, 1
Yang, Z. X., Zhang, L., Huang, Y., et al. 2022, ApJ, 937, 33
You, B., Bursa, M., & Życki, P. T. 2018, ApJ, 858, 82
You, B., Tuo, Y., Li, C., et al. 2021, NatCo, 12, 1025
Zhang, W., Tao, L., Soria, R., et al. 2022, ApJ, 927, 210
Zhu, H., Chen, X., & Wang, W. 2023, MNRAS, 523, 4394